

Finite-Width Neural Tangent Kernels from Feynman Diagrams

Max Guillen^{*a}

Philipp Misof^{*a}

Jan E. Gerken^a

Abstract

Neural tangent kernels (NTKs) are a powerful tool for analyzing deep, non-linear neural networks. In the infinite-width limit, NTKs can easily be computed for most common architectures, yielding full analytic control over the training dynamics. However, at infinite width, important properties of training such as NTK evolution or feature learning are absent. Nevertheless, finite width effects can be included by computing corrections to the Gaussian statistics at infinite width. We introduce Feynman diagrams for computing finite-width corrections to NTK statistics. These dramatically simplify the necessary algebraic manipulations and enable the computation of layer-wise recursive relations for arbitrary statistics involving preactivations, NTKs and certain higher-derivative tensors (dNTK and ddNTK) required to predict the training dynamics at leading order. We demonstrate the feasibility of our framework by extending stability results for deep networks from preactivations to NTKs and proving the absence of finite-width corrections for scale-invariant nonlinearities such as ReLU on the diagonal of the Gram matrix of the NTK. We validate our results with numerical experiments.

1 Introduction

The neural tangent kernel (NTK) is defined as $\Theta(x, x') = J(x)J(x')^\top$, where $J(x)$ is the Jacobian of the neural network evaluated at x with respect to the network parameters. Given a training dataset and loss function, the NTK completely specifies the evolution of the neural network to first order in the learning rate. This makes the NTK a powerful tool to approximate neural network training dynamics and many works have measured Θ during or after training for various applications [1, 2, 3, 4, 5]. At the same time, the NTK can also be studied theoretically. However, the NTK is a random variable via its dependence on the initialization and it evolves non-linearly during training as the parameters are updated, making direct theoretical analyses of the NTK prohibitively difficult.

Nevertheless, it is well-known that neural networks simplify considerably in the infinite-width limit, in which the number of channels of all hidden layers are taken to infinity [6, 7, 8]. In particular, the NTK collapses onto its mean and does not evolve during training, it *freezes* [9]. This deterministic NTK can be computed in closed form for deep, non-linear networks by applying layer-wise recursive relations which have been derived for all common neural network layers [10]. Therefore, both gradient descent [9] and Bayesian inference [11] can be solved in closed form at infinite width.

Although the study of the infinite-width limit has been very successful, the simplifications of the dynamics which enabled this progress also constitute an important limitation of this approach. In particular, at infinite width, the network is effectively linearized in its parameters [12] and becomes a Gaussian

^{*}Equal contribution

^aDepartment of Mathematical Sciences, Chalmers University of Technology and the University of Gothenburg, SE-412 96 Gothenburg, Sweden.

Emails: maxgui@chalmers.se, misof@chalmers.se, gerken@chalmers.se

process. Furthermore, only the last layer evolves during training, a property termed *no feature learning*. Correspondingly, some studies found considerable deviations between the properties observed for finite-width networks and those predicted by NTKs at infinite width [13, 14, 15].

A solution for this problem is to consider how deviations from the strict infinite-width limit affect the NTK statistics. In particular, one can expand the training dynamics in a Taylor series in $1/n$, where n is the width of the hidden layers [16, 17]. In this expansion, the leading term, $1/n \rightarrow 0$, corresponds to the infinite width limit and the first correction introduces finite-width effects. Including these finite-width effects in the analysis greatly extends the power of the theoretical framework which now includes non-trivial NTK statistics, the evolution of the NTK and feature learning.

Since the infinite-width statistics are Gaussian, this constitutes an expansion of the parameter statistics around a Gaussian distribution. Such an expansion is very common in theoretical physics, in particular in quantum field theory (QFT), which describes the interactions of elementary particles in a statistical manner. In perturbative QFT, the *action* (log-probability) of the theory is expanded around a leading Gaussian contribution which corresponds to non-interacting particles, while non-Gaussian corrections introduce interactions. Therefore, by employing methods from QFT, one can compute corrections to the infinite-width limit of neural network statistics. However, the algebraic manipulations involved in deriving these results are lengthy and usually phrased in a language unfamiliar to the machine-learning community. In contrast, when performing computations in particle physics, physicists mostly use *Feynman diagrams* as an intuitive shorthand to greatly simplify the computational effort.

In this article, we introduce Feynman-like diagrams for the computation of finite-width corrections to NTKs of MLPs. We provide Feynman rules for straightforwardly computing all relevant neural network statistics involving preactivations, the NTK and related quantities. In this framework, computing expectation values reduces to drawing all diagrams compatible with the desired expectation value and translating them into algebraic expressions using the Feynman rules we provide.

In order to demonstrate the power of our framework, we investigate the stability of gradients as the depth of the network increases. At infinite width, a critical initialization variance can be derived, for which the preactivations and NTK do not grow exponentially in depth. It could be shown that the same critical initialization stabilizes the forward pass also at finite width using Feynman diagrams for preactivations [18]. Using our NTK-Feynman diagrams, we can extend this result to the gradients at finite width. We also show that for scale-invariant activation functions such as ReLU, $\Theta(x, x)$ does not include finite-width corrections and the infinite-width statistics are exact.

We confirm our theoretical results with numerical experiments. By computing ensemble-averages of pre-activations and Jacobians, we demonstrate the stability of the critical initialization for statistics involving the NTK. In the same way, we confirm our stability results for scale-invariant nonlinearities.

Our main contributions are as follows:

- We provide a set of rules for computing finite-width corrections to NTK statistics using Feynman diagrams, greatly simplifying the algebraic manipulations required. We verify that our rules result in the correct layer-wise recursion relations for the NTK and preactivation statistics at order $1/\text{width}$ and find no contradictions for selected checks at higher order.
- We demonstrate the power of our formalism by deriving the recursion relation of the leading order correction to the mean of the NTK using our Feynman diagrams. We furthermore extend previous results on preactivation stability to arbitrary statistics of preactivations and the NTK. Finally, by showing that all $1/\text{width}$ corrections of $\Theta(x, x)$ vanish for scale-invariant nonlinearities, we prove that its infinite-width expression is exact in this case.
- We validate our results experimentally by sampling ensembles of MLPs. In particular, we show that the initialization variance which stabilizes the infinite-width limit also stabilizes all statistics

involving the NTK to all orders in $1/\text{width}$ by sampling 7 tensors below, at and above criticality and measuring their dependence on depth. We furthermore verify by sampling that $\Theta(x, x)$ receives no finite-width corrections for the scale-invariant activation functions ReLU and LeakyReLU but corrections are present for GeLU (not scale-invariant).

2 Related work

The analytical study of the NTK at infinite width has led to numerous insights about the training dynamics with results on trainability [19], double-descent [20], generative adversarial networks [21], physics-informed neural networks [22], data augmentation [23] and equivariant neural networks [24], among others. Infinite-width NTKs have also been used to optimize various aspects of the training process, such as architecture selection and bias detection [25].

In the machine-learning literature, finite-width corrections in the formulation used in this article were studied in [16]. A book on the subject which develops the background step-by-step and contains many novel results is also available [17]. The analogy between QFT and neural networks has been explored from different perspectives in the physics literature. It was studied systematically for the first time in [26]. This work also established a connection to renormalization group flow which was studied in a non-perturbative setting in [27]. In [28], a connection to the $O(N)$ vector model was established. Different perturbations of the infinite-width limit related to the Edgeworth expansion have been studied as well [29]. This line of work has led to results about symmetries [30], initialization stability [18], orthogonal initializations [31] and scaling laws [32, 33] among others.

Feynman diagrams appear in [18, 26, 28, 29, 32, 33], but are restricted to preactivation-statistics. In contrast, we use Feynman diagrams to compute NTK and joint preactivation-NTK statistics. This constitutes a substantial extension since preactivation statistics can only describe the initialization of the network, while NTK statistics are needed for training. Also [34] uses Feynman diagrams to study corrections to the NTK, but their treatment is restricted to providing the scaling behavior of correlation functions, whereas our framework can evaluate the correlation functions explicitly.

3 Finite-width corrections to the NTK

For an L -layer neural network $\mathcal{N} : \mathbb{R}^{n_{\text{in}}} \rightarrow \mathbb{R}^{n_{\text{out}}}$ with parameters θ , the layer- ℓ -empirical NTK is defined by

$$\widehat{\Theta}_{ij}^{(\ell)}(x, x') = \sum_{\mu} \frac{\partial z_i^{(\ell)}(x)}{\partial \theta_{\mu}} \frac{\partial z_j^{(\ell)}(x')}{\partial \theta_{\mu}}, \quad (1)$$

where $z_i^{(\ell)}$ are the channel- i preactivations of layer ℓ and we sum over all parameters in the layers $\ell' \leq \ell$. We will refer to channel indices i, j, \dots as *neural indices*. The NTK of the entire network is given by $\widehat{\Theta} = \widehat{\Theta}^{(L)}$. This kernel is highly non-linear, evolves during training and is a stochastic variable due to its dependence on the initialization. To first order in the learning rate, the training dynamics of the neural network are completely specified by the NTK. Therefore, understanding the NTK is key to understanding the training dynamics of neural networks.

While the NTK captures the correlations of the gradients of the network, the *neural network Gaussian process (NNGP) kernel*, defined by

$$\widehat{K}_{ij}^{(\ell)}(x, x') = z_i^{(\ell)}(x) z_j^{(\ell)}(x'), \quad (2)$$

captures the correlations of the preactivations. The NNGP also is a random variable due to initialization. Both kernels evolve during training, but we will consider them at initialization. Their functional forms depend on the architecture and we will restrict to MLPs for the remainder of this article.

To describe the statistics of the NTK, we introduce the *NTK fluctuations* $\widehat{\Delta\Theta}_{ij}^{(\ell)} = \widehat{\Theta}_{ij}^{(\ell)} - \mathbb{E}_\theta[\widehat{\Theta}_{ij}^{(\ell)}]$, where the expectation value is over initializations. In the infinite-width limit, in which the number n of hidden channels in \mathcal{N} goes to infinity, the NTK becomes constant in training time and collapses onto its mean [9]¹. Therefore, at infinite width, the NTK fluctuations vanish, $\widehat{\Delta\Theta} = 0$. The constant, deterministic NTK at infinite width, the *frozen* NTK, can be computed by layer-wise recursion relations for which efficient implementations exist [10].

To go beyond the infinite-width limit, one can consider a Taylor expansion of the neural network dynamics in $1/n$ [16, 17]. In this setting, the leading contribution corresponds to the Gaussian process behavior at $n \rightarrow \infty$ and higher-order corrections in $1/n$ introduce non-linear effects and feature evolution. The corrections to the NTK at higher orders are neither constant nor deterministic. The neural network statistics are then characterized by computing mixed moments of the NTK and preactivations in a given layer, for instance

$$\mathbb{E}_\theta[z_{i_1}^{(\ell)}(x_1)z_{i_2}^{(\ell)}(x_2)\widehat{\Delta\Theta}_{i_3i_4}^{(\ell)}(x_3, x_4)]. \quad (3)$$

Since $\widehat{\Delta\Theta} = 0$ at infinite width, (3) is of order $1/n$. Because higher-order moments correspond to higher orders in $1/n$, by computing finitely many mixed moments, the statistics of the relevant quantities can be described completely to a certain order in $1/n$. Instead of computing mixed moments of the form (3) directly, we will instead work with so-called *joint cumulants* (*connected correlators* in physics), denoted by \mathbb{E}^c . Intuitively, a joint cumulant is the corresponding mixed moment with all factorizations of the expectation value subtracted. A more detailed description is provided in Appendix A.

In order to extract the building blocks of the cumulants at a certain order in $1/n$, we decompose the cumulants according to their dependence on the neural indices. For instance, we introduce the tensors D and F by decomposing the cumulant of (3) as [17]

$$\begin{aligned} \mathbb{E}_\theta^c[z_{i_1}^{(\ell+1)}(x_1), z_{i_2}^{(\ell+1)}(x_2), \widehat{\Delta\Theta}_{i_3i_4}^{(\ell+1)}(x_3, x_4)] \\ = \frac{1}{n_\ell} (D_{1234}^{(\ell+1)} \delta_{i_1i_2} \delta_{i_3i_4} + F_{1324}^{(\ell+1)} \delta_{i_1i_3} \delta_{i_2i_4} + F_{1423}^{(\ell+1)} \delta_{i_1i_4} \delta_{i_2i_3}) . \end{aligned} \quad (4)$$

Here, we have highlighted the inputs x_2, x_3 appearing in the NTK in blue and $D_{\alpha\beta\gamma\delta}$ is the Gram tensor of a function D evaluated on the four inputs appearing in the cumulant, $D_{\alpha\beta\gamma\delta} = D(x_\alpha, x_\beta, x_\gamma, x_\delta)$ and similarly for F . We refer to α, β, \dots as *sample indices*. We will decompose all cumulants (and therefore moments) into such tensors according to their neural indices, as exemplified in (4). In particular, the rank-four tensors A, B, D and F together with the four-point cumulant of preactivations V_4 and the leading mean NNGP and NTK corrections $K^{\{1\}}$ and $\Theta^{\{1\}}$ completely specify the statistics of preactivations and the NTK at order $1/n$ [17]. We provide definitions of these objects in Appendix B. In order to compute $1/n$ corrections to the training dynamics, the higher-derivative tensors $dNTK$ and $ddNTK$ are necessary. These will be decomposed into the tensors P, Q, R, S, T and U [17], also defined in Appendix B.

For a given neural network, these tensors can be computed from layer-wise recursive relations, for instance F satisfies the relation [17]

$$\begin{aligned} F_{1324}^{(\ell+1)} &= (C_W^{(\ell+1)})^2 \langle \sigma_1^{(\ell)} \sigma_2^{(\ell)} \sigma_3'^{(\ell)} \sigma_4'^{(\ell)} \rangle_{K^{(\ell)}} \Theta_{34}^{(\ell)} \\ &+ \frac{n_\ell}{n_{\ell-1}} (C_W^{(\ell+1)})^2 \sum_{\alpha, \beta, \gamma, \delta=1}^4 \langle \sigma_1^{(\ell)} \sigma_3'^{(\ell)} z_\alpha^{(\ell)} \rangle_{K^{(\ell)}} \langle \sigma_2^{(\ell)} \sigma_4'^{(\ell)} z_\beta^{(\ell)} \rangle_{K^{(\ell)}} K_{(\ell)}^{\alpha\gamma} K_{(\ell)}^{\beta\delta} F_{\gamma 3 \delta 4}^{(\ell)} + \mathcal{O}\left(\frac{1}{n}\right) \end{aligned} \quad (5)$$

¹This requires an appropriate parametrization of the neural network layers, for instance the so-called neural-tangent parametrization.

where the right-hand side only involves expectation values at layer ℓ . Here, $C_W^{(\ell)}$ is the variance of the initialization distribution of the weights in layer ℓ and $K_{\alpha\beta}^{(\ell)} = K^{(\ell)}(x_\alpha, x_\beta) = \mathbb{E}_\theta[\widehat{K}^{(\ell)}(x_\alpha, x_\beta)]$ is the Gram matrix of the mean of the NNGP (similarly for Θ). \widehat{K} with upper indices denotes the inverse of the matrix $K_{\alpha\beta}$, i.e. $\sum_{\beta=1}^4 K_{(\ell)}^{\alpha\beta} K_{\beta\gamma}^{(\ell)} = \delta_{\alpha\gamma}$. By $\langle \cdot \rangle_{K^{(\ell)}}$ we denote the Gaussian expectation value with mean zero and covariance given by the matrix $K_{\alpha\beta}^{(\ell)}$. We used the shorthands $z_\alpha = z(x_\alpha)$ and $\sigma_\alpha = \sigma(z(x_\alpha))$. The prime designates the derivative of the activation function.

Unfortunately, arriving at such recursions is algebraically very laborious, hindering adoption of these expansions for machine-learning research. In this work, we introduce a framework for substantially simplifying these computations by using a graphical approach based on Feynman diagrams, allowing for the straightforward derivation of known and novel recursions such as the one discussed in Section 5.1.

4 Feynman diagrams for NTKs

Feynman diagrams are a standard tool to compute cumulants of quantum fields in theoretical particle physics. The probability distributions of these fields are Gaussians (corresponding to non-interacting particles) plus small, non-Gaussian corrections (corresponding to interactions). Feynman diagrams are graphs which symbolize these interactions. The set of *Feynman rules* defines the vertices and edges which can appear in the graphs, what order in the expansion parameter (here: $1/n$) they carry and explains how to translate a given diagram into a mathematical term. The *external vertices* correspond to the variables over which we take the expectation value and the computation proceeds by drawing all diagrams compatible with the given external vertices and the desired order according to the Feynman rules. The final result is obtained by summing up all the terms corresponding to the admissible Feynman diagrams.

4.1 The Feynman rules for NTK statistics

The set of Feynman rules for computing cumulants of preactivations was explicitly derived in [18] from first principles. This approach relied heavily on the Gaussian nature of the conditional probability distribution $P(z^{(\ell+1)}|z^{(\ell)})$. Since the NTK is quadratic in the weights, their method is no longer admissible for evaluating cumulants involving the NTK. For this reason, we will adopt an alternative strategy based on the decomposition of the cumulants into rank-four tensors as described below (4). In the following, we give an overview of the most important Feynman rules to provide a general idea of how Feynman diagrams are constructed in this context and translated into algebraic expressions. The full set of rules is provided in Appendix C.

- (i) External vertices (which correspond to the quantities which appear in the expectation value) are represented by filled dots. *Solid* and *dotted external lines* represent preactivations and NTK fluctuations, respectively

$$z_\alpha \equiv \alpha \bullet \text{---} \quad \widehat{\Delta\Theta}_{\alpha\beta} \equiv \begin{matrix} \beta \bullet \text{---} \\ \alpha \bullet \text{---} \end{matrix} \quad (6)$$

We will use different colors for external dotted lines corresponding to different NTKs. As detailed in Appendix C, additional lines represent the higher derivative terms inside the dNTK and ddNTK.

- (ii) The external lines from (6) are attached to *cubic interactions*, which are vertices connected to two external lines and one *internal line*. For cubic interactions involving external NTK lines, we introduce the following Feynman rules

$$\begin{matrix} \beta \bullet \\ \alpha \bullet \end{matrix} \text{---} \widehat{\Delta\Omega}_{i,\alpha\beta}^{(\ell+1)} \sim \frac{1}{n_\ell} \begin{matrix} \beta \bullet \\ \alpha \bullet \end{matrix} \text{---} \sigma_{i,\alpha}^{(\ell)} \sigma_{i,\beta}^{(\ell)} \sim \frac{C_W^{(\ell+1)}}{n_\ell} \begin{matrix} \beta \bullet \\ \alpha \bullet \end{matrix} \text{---} \sigma_{i,\alpha}^{\prime(\ell)} \sigma_{i,\beta}^{\prime(\ell)} \sim \frac{C_W^{(\ell+1)}}{n_\ell} \begin{matrix} \beta \bullet \\ \alpha \bullet \end{matrix} \text{---} \sigma_{i,\alpha}^{\prime(\ell)} \sigma_{i,\beta}^{\prime(\ell)} \sim \frac{C_W^{(\ell+1)}}{n_\ell} \begin{matrix} \beta \bullet \\ \alpha \bullet \end{matrix} \text{---} \sigma_{i,\alpha}^{\prime(\ell)} \sigma_{i,\beta}^{\prime(\ell)} \quad (7)$$

where $\widehat{\Delta\Omega}_{i,\alpha\beta}^{(\ell+1)} = \sigma_{i,\alpha}^{(\ell)}\sigma_{i,\alpha}^{(\ell)} + C_W^{(\ell+1)}\Theta_{\alpha\beta}^{(\ell)}\sigma_{i,\alpha}'^{(\ell)}\sigma_{i,\beta}'^{(\ell)}$. The line without dot is the internal line. We discuss its decoration in the next Feynman rule. Additional cubic vertices for preactivation, dNTK and ddNTK lines are provided in Appendix C.

- (iii) The internal lines from the vertices (42) are connected to a *propagator* which will be represented by a white blob

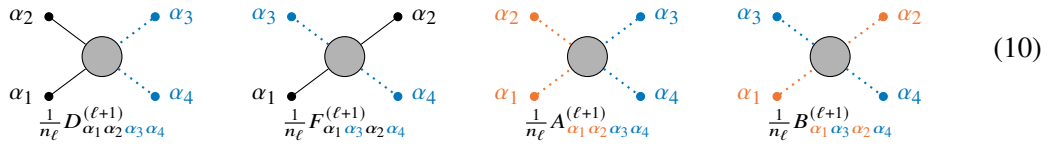
$$\langle \rangle_{K^{(\ell)}} \equiv \bigcirc \quad (8)$$

where $\langle \rangle_{K^{(\ell)}}$ stands for a Gaussian expectation value with mean zero and covariance given by the Gram matrix of the NNGP, as in (5). We take the expectation value over the decorations of the internal lines attached to the propagator, for instance

$$\widehat{\Delta\Omega}_{i,\alpha\beta} \widehat{\Delta\Omega}_{i,\gamma\delta} \sim \langle \widehat{\Delta\Omega}_{i,\alpha\beta} \widehat{\Delta\Omega}_{i,\gamma\delta} \rangle_{K^{(\ell)}}. \quad (9)$$

Propagators obey *selection rules*, special properties regarding how lines are allowed to connect to them, see Appendix C for details.

- (iv) The 10 rank-four tensors into which we decompose the cumulants will be represented by *quartic interactions* with four external lines. We introduce the following quartic vertices containing NTK and preactivation lines



$$\begin{array}{cccc} \alpha_2 & \alpha_3 & \alpha_3 & \alpha_2 \\ \alpha_1 & \alpha_4 & \alpha_1 & \alpha_4 \\ \frac{1}{n_\ell} D_{\alpha_1 \alpha_2 \alpha_3 \alpha_4}^{(\ell+1)} & \frac{1}{n_\ell} F_{\alpha_1 \alpha_3 \alpha_2 \alpha_4}^{(\ell+1)} & \frac{1}{n_\ell} A_{\alpha_1 \alpha_2 \alpha_3 \alpha_4}^{(\ell+1)} & \frac{1}{n_\ell} B_{\alpha_1 \alpha_3 \alpha_2 \alpha_4}^{(\ell+1)} \end{array} \quad (10)$$

The quartic vertices can also appear with four internal lines instead. In this case, they correspond to tensors in layer ℓ instead of $\ell + 1$ and are connected to propagators. Further quartic tensors for the remaining tensors involving preactivations, the dNTK and ddNTK are introduced in Appendix B. For the mean NNGP and NTK corrections $K^{\{1\}}$ and $\Theta^{\{1\}}$, we similarly introduce *quadratic vertices* of valence two.

- (v) Internal lines attached to cubic or internal quartic vertices have unassigned neural indices (e.g. i in the vertices in (42)). Similarly, internal (solid) preactivation lines have unassigned sample indices. To assemble the term corresponding to a certain diagram, multiply the expressions corresponding to vertices and propagators and sum over all unassigned neural and sample indices. The complete expression for a cumulant is given by summing over all Feynman diagrams with the correct external lines and order in $1/n$.

In Appendix C, we provide extensive comparisons of recursion relations computed from these rules and show that our Feynman rules indeed yield the correct results.

4.2 Recursion relation for F

To illustrate how to use our Feynman rules, we will reproduce the recursion relation (5) from Feynman diagrams in this section.

The layer- $(\ell + 1)$ tensor on the LHS of (5) is given by the second quartic vertex in (10). We will now proceed to draw all Feynman diagrams which have the same external lines as this quartic vertex and are of order $1/n$. First, we notice that the only way to combine a dotted (NTK) line with a solid (preactivation) line in a cubic vertex is to use the second vertex in (42). We use this vertex twice (for inputs 1, 3 and 2, 4, respectively). One then obtains two internal solid-dashed lines, each decorated with $\sigma_i^{(\ell)}\sigma_i'^{(\ell)}$. This,

in turn, gives rise to two possibilities: The input channels for both lines can either be equal or different. If the input channels are equal, they can be connected directly by a propagator. If they are different, they can be connected by introducing two propagators and an internal F -tensor in layer ℓ . The diagrams corresponding to the expression (5) are therefore

$$\begin{array}{c} 3 \\ \bullet \\ \vdots \\ 1 \end{array} \begin{array}{c} \bullet \\ \vdots \\ 2 \\ \bullet \end{array} = \sum_j \begin{array}{c} 3 \\ \bullet \\ \vdots \\ 1 \end{array} \begin{array}{c} \bullet \\ \vdots \\ 2 \\ \bullet \end{array} + \sum_{j_1, j_2} \begin{array}{c} 3 \\ \bullet \\ \vdots \\ 1 \end{array} \begin{array}{c} \bullet \\ \vdots \\ 2 \\ \bullet \end{array} \quad (11)$$

Here, we have added the necessary sums over unassigned neural indices. No more diagrams can be constructed because these would either be at higher order in $1/n$ or be ruled out by the selection rules of the propagator detailed in Appendix C. With these rules, one can check that the first and second diagrams on the RHS of (11) correspond to the first and second terms in (5), respectively.

5 Applications

In this section, we will describe three applications of our Feynman rules to problems in deep learning.

5.1 Recursion relation for the NTK mean

Using our Feynman rules, it is straightforward to compute even complicated recursion relations. To demonstrate this, we will compute the recursion relation for the first-order correction in $1/n$ of the NTK mean $\Theta^{\{1\}}$, which, to the best of our knowledge, has not been derived before. Starting from the quadratic vertex $1 \bullet \dots \bullet 2$ representing $\Theta_{12}^{\{1\}}/n_\ell$, we draw all Feynman diagrams with two external NTK lines at order $1/n$. The Feynman rules (42) and (10) as well as the selection rules of the propagator imply the existence of five diagrams for such a tensor $\Theta_{12}^{\{1\}(\ell+1)}$: Two diagrams contain the quadratic vertices of $K^{\{1\}}$ and $\Theta^{\{1\}}$ at layer ℓ , the other three diagrams contain the quartic vertices for D , F and V_4 . Explicitly,

$$\begin{array}{c} 1 \\ \bullet \\ \vdots \\ 1 \end{array} \begin{array}{c} \bullet \\ \vdots \\ 2 \\ \bullet \end{array} = \frac{1}{n_{\ell-1}} \Theta_{12}^{\{1\}(\ell)} + \frac{1}{n_{\ell-1}} K_{12}^{\{1\}(\ell)} + \frac{1}{n_{\ell-1}} V_4^{(\ell)} + \frac{1}{n_{\ell-1}} D_4^{(\ell)} + \frac{1}{n_{\ell-1}} F_4^{(\ell)} \quad (12)$$

The algebraic expression corresponding to (12) is given in Appendix E.

5.2 Gradient stability at finite width

Stabilizing against exploding or vanishing preactivations and gradients is of central importance in deep learning [35, 36]. Analyzing the *susceptibility* χ , the growth factor of the NNGP [37] and NTK [19] from layer to layer, at infinite width yields an activation-function dependent phase diagram for the initialization variances of weights and biases. At criticality, when gradients and preactivations neither grow nor vanish exponentially, $\chi = 1$. Recently, the analysis of preactivation stability has been expanded to finite-width. In particular, [18] could show that all higher-order statistics of preactivations at finite width are at criticality if the infinite width is at criticality. Therefore, the forward pass is also stable at finite width. In this section, we will extend this result to statistics involving the NTK, i.e. to the backward pass.

The criticality of a tensor can be analyzed by computing how variations of the tensors in layer ℓ lead to variations at layer $\ell+1$ [17, 18]. We will therefore use our Feynman rules to study the variations of tensors

where $(\chi_{\parallel}^{(\ell+1)})_{\alpha\beta,\gamma\delta} = \frac{C_W^{(\ell+1)}}{2} \langle \frac{d^2(\sigma_{\alpha}\sigma_{\beta})}{dz_{\gamma}dz_{\delta}} \rangle_{K^{(\ell)}} = \delta_{\alpha\gamma}\delta_{\beta\delta}$ at criticality [18], setting the prefactor in (19) to 1. Once more, one finds that the criticality conditions entirely determine the stability of the higher-rank F tensor. A similar argument for the higher-rank D -tensors can be found in Appendix F.

The leading-order contributions to the rank- k contributions are $O(1/n^{(k-2)/2})$. However, since the internal lines and propagators at leading order already exhaust all possible contributions to the variations and these were set to 1 by the infinite-width criticality conditions, we conclude that all higher order contributions to the tensors discussed here are stabilized as well. A similar analysis for the tensors A and B and their higher-rank generalizations can be found in Appendix F. Therefore, all preactivation- and NTK statistics are stabilized to all orders in $1/n$. This analysis demonstrates how the NTK Feynman rules can be used to arrive at powerful all-order results.

5.3 Absence of NTK-corrections for ReLU

Scale-invariant nonlinearities satisfy $\sigma(\lambda z) = \lambda \sigma(z)$ for $\lambda > 0$. Important examples include ReLU and LeakyReLU. Remarkably, these activation functions have the property that their NNKP does not receive finite-width corrections for equal inputs, so the infinite-width result is valid for finite-width networks as well, $\widehat{K}(x, x) = K(x, x)$ [17].

In this section, we will establish a similar result for the finite-width correction of the NTK mean for MLPs with scale-invariant nonlinearities. For the special case of ReLU, this fact was proven before, using different techniques [38, 39]. To obtain the same result for all scale-invariant activation functions using Feynman diagrams, we will separately evaluate the algebraic expressions of the last four diagrams in (12) to show that they all vanish for the case under discussion: The first of those does not contribute since $K^{\{1\}(\ell)} = 0$ for scale-invariant activation functions. The second diagram vanishes due to the property

$$2K^2 \frac{d}{dK} \left[2K^2 \frac{d}{dK} \langle \widehat{\Delta\Omega}(z) \rangle_K \right] - 8K^3 \frac{d}{dK} \langle \widehat{\Delta\Omega}(z) \rangle_K = 0 \quad (20)$$

satisfied by the kernel $K = K(x, x)$ of scale-invariant activation functions, see Appendix G for a proof. Finally, the third and fourth diagrams in (12) vanish as a consequence of

$$\langle \sigma'(z)\sigma'(z)(z^2 - K) \rangle_K = 2K^2 \frac{d}{dK} \langle \sigma'(z)\sigma'(z) \rangle_K \quad (21)$$

and the fact that $\langle \sigma'(z)\sigma'(z) \rangle_K$ is a constant for scale-invariant nonlinearities, see Appendix G for a proof. Therefore, the only diagram which contributes on the RHS of (21) is that proportional to $\Theta^{\{1\}}$. Since the first-layer NTK mean does not develop any finite-width correction, one concludes by induction that the NTK mean does not receive finite-width corrections for scale-invariant nonlinearities.

6 Experiments

In this section, we summarize our numerical experiments which verify the results from Section 5.

6.1 Gradient stability

We verify numerically for finite-width ReLU-MLPs that the preactivation and NTK statistics are stabilized for the critical initialization $C_W^{(\ell)} = C_W^c = 2$, whereas larger (lower) values lead to exponential growth (decay) with depth. In particular, we compute the ensemble average $\overline{\Theta}_{\alpha\beta}^{(\ell)} = \frac{1}{N_{\text{net}}} \sum_{I=1}^{N_{\text{net}}} \widehat{\Theta}_{I,\alpha\beta}^{(\ell)}$ of (1) for up to 30 layers to approximate the mean NTK $\Theta_{\alpha\beta}$. Here, I labels the independent initializations. Figure 1

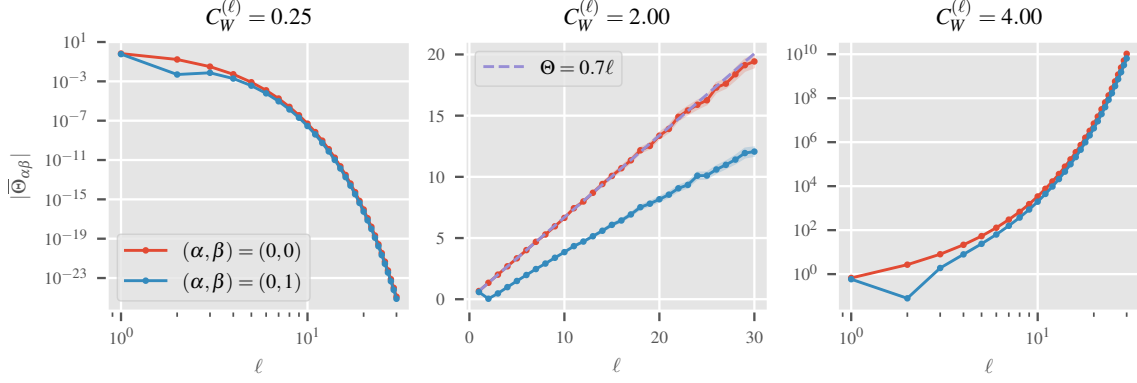


Figure 1: *Gradient stability*. Components of the Monte–Carlo estimated NTK $\bar{\Theta}_{\alpha\beta}$ of a ReLU MLP as a function of layer depth ℓ corresponding to single and distinct inputs are shown for three different choices of $C_W^{(\ell)}$. The hidden layers are of size 200. The case for the critical value $C_W^{(\ell)} = C_W^c = 2$ is shown in the middle. For the single input case at criticality (red line in the middle), we also show the expected linear relation [17] (purple). Sample means are obtained from 1000 initializations. Error bands are standard errors of the mean but mostly too small to be visible.

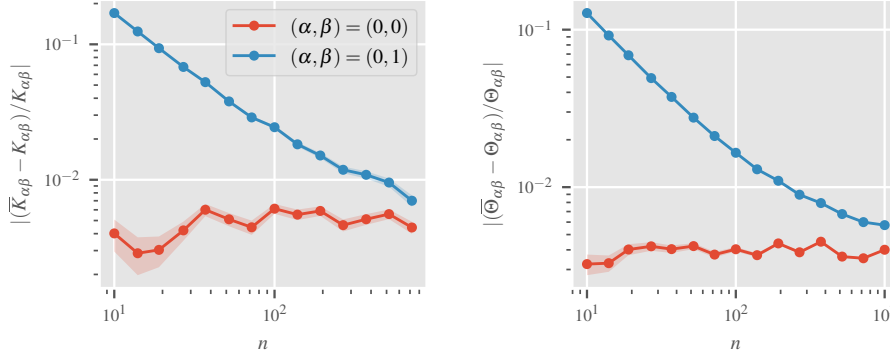


Figure 2: *Finite-width corrections for ReLU*. Relative deviations of the Monte–Carlo estimated NNGP and NTK to its infinite-width counterparts as a function of hidden layer width $n = n_\ell$. A four layer ReLU MLP with $C_W = 2$ is sampled over 5×10^6 initializations. Error bars of the sample mean are included for all lines. Both a single and distinct input component of each kernel is shown.

shows the linear scaling for both the single and the distinct input case when $C_W^{(\ell)} = C_W^c$, in contrast to the exponential behavior observed away from this value. In Appendix H we provide further details and also numerically verify the simultaneous stability of the NNGP K , the four-point cumulant V_4 and the tensors A, B, D and F which together describe the complete preactivation and NTK statistics up to rank four.

6.2 Absence of kernel-corrections for scale-invariant activations

We measure the finite-width corrections to the infinite-width NTK by computing the relative deviation $|(\bar{\Theta}_{\alpha\beta} - \Theta_{\alpha\beta})/\Theta_{\alpha\beta}|$ of the ensemble average to the frozen NTK (computed with the `neural-tangents` library [10]) at different hidden-layer widths $n = n_\ell$. The NNGP corrections are investigated analogously. The results for the single and distinct input case are shown in Figure 2. Indeed, the single input component does not receive corrections, while the distinct input case only approaches the infinite-width result as $n \rightarrow \infty$. For further details, we refer to Appendix H, where we also check the absence of corrections for LeakyReLU and show that the kernels do receive corrections for GeLU, which is not scale-invariant.

7 Limitations

Although the framework of computing finite-width corrections to the NTK applies to very general architectures, we have restricted our attention here to MLPs. Extensions to other architectures would require a modification of the Feynman rules, but we see no conceptual obstacle to doing so.

Furthermore, our analysis was mostly restricted to order $1/n$. The discussion in Section 5.2 involves all orders in $1/n$ and shows examples of the higher-rank generalizations of the tensors appearing at higher order in $1/n$. We expect such straightforward generalizations to be able to capture all orders in $1/n$, and have performed further tests at order $1/n^2$ which showed no contradictions, see Appendix I. However, a full analysis of higher-order tensors is beyond the scope of this work.

References

- [1] Jonathan Hayase and Sewoong Oh. “Few-Shot Backdoor Attacks via Neural Tangent Kernels”. In: *The Eleventh International Conference on Learning Representations*. Sept. 2022. arXiv: [2210.05929](#).
- [2] Jisoo Mok et al. “Demystifying the Neural Tangent Kernel from a Practical Perspective: Can It Be Trusted for Neural Architecture Search without Training?” In: *2022 IEEE/CVF Conference on Computer Vision and Pattern Recognition (CVPR)*. June 2022, pp. 11851–11860. doi: [10.1109/CVPR52688.2022.01156](#). arXiv: [2203.14577](#).
- [3] Andrew William Engel et al. “Faithful and Efficient Explanations for Neural Networks via Neural Tangent Kernel Surrogate Models”. In: *The Twelfth International Conference on Learning Representations*. Oct. 2023. arXiv: [2305.14585](#).
- [4] Qiqi Zhou and Yichen Zhu. “When Training-Free Nas Meets Vision Transformers: A Neural Tangent Kernel Perspective”. In: *ICASSP 2024 - 2024 IEEE International Conference on Acoustics, Speech and Signal Processing (ICASSP)*. Apr. 2024, pp. 7405–7409. doi: [10.1109/ICASSP48485.2024.10447479](#). arXiv: [2405.04536](#).
- [5] Joseph Wilson et al. *Uncertainty Quantification with the Empirical Neural Tangent Kernel*. Feb. 2025. arXiv: [2502.02870](#).
- [6] Radford M. Neal. *Bayesian Learning for Neural Networks*. Springer Science & Business Media, 1996. ISBN: 978-1-4612-0745-0.
- [7] Jaehoon Lee et al. “Deep Neural Networks as Gaussian Processes”. In: *International Conference on Learning Representations*. Feb. 2018. arXiv: [1711.00165](#).
- [8] Alexander G. de G. Matthews et al. “Gaussian Process Behaviour in Wide Deep Neural Networks”. In: *International Conference on Learning Representations*. Feb. 2018. arXiv: [1804.11271](#).
- [9] Arthur Jacot, Franck Gabriel, and Clement Hongler. “Neural Tangent Kernel: Convergence and Generalization in Neural Networks”. In: *Advances in Neural Information Processing Systems*. Vol. 31. Curran Associates, Inc., 2018. arXiv: [1806.07572](#).
- [10] Roman Novak et al. “Neural Tangents: Fast and Easy Infinite Neural Networks in Python”. In: *Eighth International Conference on Learning Representations*. Apr. 2020. arXiv: [1912.02803](#).
- [11] Bobby He, Balaji Lakshminarayanan, and Yee Whye Teh. “Bayesian Deep Ensembles via the Neural Tangent Kernel”. In: *Advances in Neural Information Processing Systems*. Vol. 33. Curran Associates, Inc., 2020, pp. 1010–1022. arXiv: [2007.05864](#).
- [12] Jaehoon Lee et al. “Wide Neural Networks of Any Depth Evolve as Linear Models Under Gradient Descent”. In: *Advances in Neural Information Processing Systems*. Vol. 32. Curran Associates, Inc., 2019. doi: [10.1088/1742-5468/abc62b](#). arXiv: [1902.06720](#).
- [13] Jaehoon Lee et al. “Finite versus Infinite Neural Networks: An Empirical Study”. In: *Advances in Neural Information Processing Systems*. Ed. by H. Larochelle et al. Vol. 33. Curran Associates, Inc., 2020, pp. 15156–15172. arXiv: [2007.15801](#).
- [14] Jonathan Wenger, Felix Dangel, and Agustinus Kristiadi. *On the Disconnect Between Theory and Practice of Neural Networks: Limits of the NTK Perspective*. May 2024. arXiv: [2310.00137](#).
- [15] Haoran Liu et al. *Issues with Neural Tangent Kernel Approach to Neural Networks*. Jan. 2025. arXiv: [2501.10929](#).
- [16] Sho Yaida. “Non-Gaussian Processes and Neural Networks at Finite Widths”. In: *Proceedings of The First Mathematical and Scientific Machine Learning Conference*. PMLR, Aug. 2020, pp. 165–192. arXiv: [1910.00019](#).

- [17] Daniel A. Roberts and Sho Yaida. *The Principles of Deep Learning Theory: An Effective Theory Approach to Understanding Neural Networks*. Cambridge: Cambridge University Press, 2022. ISBN: 978-1-316-51933-2. DOI: [10.1017/9781009023405](#). arXiv: [2106.10165](#).
- [18] Ian Banta et al. “Structures of Neural Network Effective Theories”. In: *Physical Review D* 109.10 (May 2024), p. 105007. DOI: [10.1103/PhysRevD.109.105007](#). arXiv: [2305.02334](#).
- [19] Lechao Xiao, Jeffrey Pennington, and Samuel Schoenholz. “Disentangling Trainability and Generalization in Deep Neural Networks”. In: *Proceedings of the 37th International Conference on Machine Learning*. PMLR, Nov. 2020, pp. 10462–10472. arXiv: [1912.13053](#).
- [20] Mario Geiger et al. “Scaling Description of Generalization with Number of Parameters in Deep Learning”. In: *Journal of Statistical Mechanics: Theory and Experiment* 2020.2 (Feb. 2020), p. 023401. ISSN: 1742-5468. DOI: [10.1088/1742-5468/ab633c](#).
- [21] Jean-Yves Franceschi et al. “A Neural Tangent Kernel Perspective of GANs”. In: *Proceedings of the 39th International Conference on Machine Learning*. PMLR, June 2022, pp. 6660–6704. DOI: [10.48550/arXiv.2106.05566](#). arXiv: [2106.05566](#).
- [22] Sifan Wang, Xinling Yu, and Paris Perdikaris. “When and Why PINNs Fail to Train: A Neural Tangent Kernel Perspective”. In: *Journal of Computational Physics* 449 (Jan. 2022), p. 110768. ISSN: 0021-9991. DOI: [10.1016/j.jcp.2021.110768](#).
- [23] Jan E. Gerken and Pan Kessel. “Emergent Equivariance in Deep Ensembles”. In: *Proceedings of the 41st International Conference on Machine Learning*. PMLR, July 2024, pp. 15438–15465. arXiv: [2403.03103](#).
- [24] Philipp Misof, Pan Kessel, and Jan E. Gerken. “Equivariant Neural Tangent Kernels”. In: *Proceedings of the 42nd International Conference on Machine Learning*. PMLR, 2025. arXiv: [2406.06504](#).
- [25] Joshua DeOliveira, Walter Gerych, and Elke Rundensteiner. “The Surprising Effectiveness of Infinite-Width NTKs for Characterizing and Improving Model Training”. In: *Proceedings of the AAAI Conference on Artificial Intelligence*. Vol. 39. Apr. 2025, pp. 16262–16270. DOI: [10.1609/aaai.v39i15.33786](#).
- [26] James Halverson, Anindita Maiti, and Keegan Stoner. “Neural Networks and Quantum Field Theory”. In: *Machine Learning: Science and Technology* 2.3 (Sept. 2021), p. 035002. ISSN: 2632-2153. DOI: [10.1088/2632-2153/abeca3](#). arXiv: [2008.08601](#).
- [27] Harold Erbin, Vincent Lahoche, and Dine Ousmane Samary. “Nonperturbative Renormalization for the Neural Network-QFT Correspondence”. In: *Machine Learning: Science and Technology* 3.1 (Mar. 2022), p. 015027. ISSN: 2632-2153. DOI: [10.1088/2632-2153/ac4f69](#). arXiv: [2108.01403](#).
- [28] Kevin Grosvenor and Ro Jefferson. “The Edge of Chaos: Quantum Field Theory and Deep Neural Networks”. In: *SciPost Physics* 12.3 (Mar. 2022), p. 081. ISSN: 2542-4653. DOI: [10.21468/SciPostPhys.12.3.081](#). arXiv: [2109.13247](#).
- [29] Mehmet Demirtas et al. “Neural Network Field Theories: Non-Gaussianity, Actions, and Locality”. In: *Machine Learning: Science and Technology* 5.1 (Jan. 2024), p. 015002. ISSN: 2632-2153. DOI: [10.1088/2632-2153/ad17d3](#). arXiv: [2307.03223](#).
- [30] Anindita Maiti, Keegan Stoner, and James Halverson. “Symmetry-via-Duality: Invariant Neural Network Densities from Parameter-Space Correlators”. In: *Machine Learning in Pure Mathematics and Theoretical Physics*. Chap. Chapter 8, pp. 293–330. DOI: [10.1142/9781800613706_0008](#).
- [31] Hannah Day, Yonatan Kahn, and Daniel A. Roberts. *Feature Learning and Generalization in Deep Networks with Orthogonal Weights*. Oct. 2023. arXiv: [2310.07765](#).
- [32] Alexander Maloney, Daniel A. Roberts, and James Sully. *A Solvable Model of Neural Scaling Laws*. Oct. 2022. arXiv: [2210.16859](#).
- [33] Zhengkang Zhang. “Neural Scaling Laws from Large-N Field Theory: Solvable Model beyond the Ridgeless Limit”. In: *Machine Learning: Science and Technology* 6.2 (Apr. 2025), p. 025010. ISSN: 2632-2153. DOI: [10.1088/2632-2153/adc872](#). arXiv: [2405.19398](#).
- [34] Ethan Dyer and Guy Gur-Ari. “Asymptotics of Wide Networks from Feynman Diagrams”. In: *International Conference on Learning Representations*. Sept. 2019. arXiv: [1909.11304](#).
- [35] Xavier Glorot and Yoshua Bengio. “Understanding the Difficulty of Training Deep Feedforward Neural Networks”. In: *Proceedings of the Thirteenth International Conference on Artificial Intelligence and Statistics*. JMLR Workshop and Conference Proceedings, Mar. 2010, pp. 249–256.
- [36] Kaiming He et al. “Delving Deep into Rectifiers: Surpassing Human-Level Performance on ImageNet Classification”. In: *Proceedings of the IEEE International Conference on Computer Vision*. 2015, pp. 1026–1034. arXiv: [1502.01852](#).
- [37] Ben Poole et al. “Exponential Expressivity in Deep Neural Networks through Transient Chaos”. In: *Advances in Neural Information Processing Systems*. Vol. 29. Curran Associates, Inc., 2016.
- [38] Boris Hanin and Mihai Nica. “Finite Depth and Width Corrections to the Neural Tangent Kernel”. In: *International Conference on Learning Representations*. Sept. 2019. arXiv: [1909.05989](#).

- [39] Mariia Seleznova and Gitta Kutyniok. “Neural Tangent Kernel Beyond the Infinite-Width Limit: Effects of Depth and Initialization”. In: *Proceedings of the 39th International Conference on Machine Learning*. PMLR, June 2022, pp. 19522–19560. arXiv: [2202.00553](#).
- [40] V. P. Leonov and A. N. Shiryaev. “On a Method of Calculation of Semi-Invariants”. In: *Theory of Probability & Its Applications* 4.3 (Jan. 1959), pp. 319–329. issn: 0040-585X. doi: [10.1137/1104031](#).

A Cumulants versus moments

Joint cumulants are generated by the logarithm of the moment generating function. By expanding these generating functions, one arrives at the moment-cumulants formula [40], which specifies how a mixed moment is expanded in terms of joint cumulants,

$$\mathbb{E}[X_1 \cdots X_n] = \sum_{p \in P_n} \prod_{b \in p} \mathbb{E}^c \left[\prod_{i \in b} X_i \right], \quad (22)$$

where P_n is the set of partitions of $\{1, \dots, n\}$, hence b is a block in the partition p . For instance,

$$\begin{aligned} \mathbb{E}[X_1 X_2 X_3] &= \mathbb{E}^c[X_1, X_2, X_3] + \mathbb{E}^c[X_1, X_2] \mathbb{E}^c[X_3] + \mathbb{E}^c[X_1, X_3] \mathbb{E}^c[X_2] + \mathbb{E}^c[X_2, X_3] \mathbb{E}^c[X_1] \\ &\quad + \mathbb{E}^c[X_1] \mathbb{E}^c[X_2] \mathbb{E}^c[X_3]. \end{aligned} \quad (23)$$

We will use the decomposition (22) to expand mixed moments in terms of cumulants which we then compute using Feynman diagrams.

Intuitively, joint cumulants correspond to subtracting all factorizations of the mixed moment, e.g.

$$\begin{aligned} \mathbb{E}^c[X_1, X_2, X_3] &= \mathbb{E}[X_1 X_2 X_3] - \mathbb{E}[X_1 X_2] \mathbb{E}[X_3] - \mathbb{E}[X_1 X_3] \mathbb{E}[X_2] - \mathbb{E}[X_2 X_3] \mathbb{E}[X_1] \\ &\quad + 2 \mathbb{E}[X_1] \mathbb{E}[X_2] \mathbb{E}[X_3], \end{aligned} \quad (24)$$

where the last term is added twice to compensate for the factorizations in the three terms before. In general, a joint cumulant is given in terms of mixed moments by [40]

$$\mathbb{E}^c[X_1, \dots, X_n] = \sum_{p \in P_n} (|p| - 1)! (-1)^{|p|-1} \prod_{b \in p} \mathbb{E} \left[\prod_{i \in b} X_i \right], \quad (25)$$

where $|p|$ is the number of blocks in the partition p .

B Definitions of all tensors

In this section, we provide the definitions for all tensors relevant in this work beyond the NNGP (2) and the NTK (1).

The means of the NNGP and NTK receive finite-width corrections which are denoted by

$$\mathbb{E}[\widehat{K}_{\alpha_1 \alpha_2}^{(\ell)}] = K_{\alpha_1 \alpha_2}^{(\ell)} + \frac{1}{n_{\ell-1}} K_{\alpha_1 \alpha_2}^{\{1\}(\ell)} + O\left(\frac{1}{n^2}\right) \quad (26)$$

$$\mathbb{E}[\widehat{\Theta}_{\alpha_1 \alpha_2}^{(\ell)}] = \Theta_{\alpha_1 \alpha_2}^{(\ell)} + \frac{1}{n_{\ell-1}} \Theta_{\alpha_1 \alpha_2}^{\{1\}(\ell)} + O\left(\frac{1}{n^2}\right), \quad (27)$$

where the unhatted quantities correspond to the infinite-width limits. The cumulant of four preactivations decomposes into the V_4 tensor, defining it according to

$$\begin{aligned} \mathbb{E}_\theta^c \left[z_{i_1; \alpha_1}^{(\ell)}, z_{i_2; \alpha_2}^{(\ell)}, z_{i_3; \alpha_3}^{(\ell)}, z_{i_4; \alpha_4}^{(\ell)} \right] &= \frac{1}{n_{\ell-1}} \left[\delta_{i_1 i_2} \delta_{i_3 i_4} V_{\alpha_1 \alpha_2 \alpha_3 \alpha_4}^{(\ell)} + \delta_{i_1 i_3} \delta_{i_2 i_4} V_{\alpha_1 \alpha_3 \alpha_2 \alpha_4}^{(\ell)} \right. \\ &\quad \left. + \delta_{i_1 i_4} \delta_{i_2 i_3} V_{\alpha_1 \alpha_4 \alpha_2 \alpha_3}^{(\ell)} \right]. \end{aligned} \quad (28)$$

The cumulant of two NTK fluctuations decomposes into the A and B tensors,

$$\begin{aligned} \mathbb{E}_\theta^c \left[\widehat{\Delta \Theta}_{i_1 i_2; \alpha_1 \alpha_2}^{(\ell)}, \widehat{\Delta \Theta}_{i_3 i_4; \alpha_3 \alpha_4}^{(\ell)} \right] &= \frac{1}{n_{\ell-1}} \left[\delta_{i_1 i_2} \delta_{i_3 i_4} A_{\alpha_1 \alpha_2 \alpha_3 \alpha_4}^{(\ell)} + \delta_{i_1 i_3} \delta_{i_2 i_4} B_{\alpha_1 \alpha_3 \alpha_2 \alpha_4}^{(\ell)} \right. \\ &\quad \left. + \delta_{i_1 i_4} \delta_{i_2 i_3} B_{\alpha_1 \alpha_4 \alpha_2 \alpha_3}^{(\ell)} \right]. \end{aligned} \quad (29)$$

In order to consistently analyze the training dynamics to order $1/n$, the following higher-derivative analogues of the NTK are necessary [17]

$$\widehat{\text{d}\Theta}_{i_0 i_1 i_2; \delta_0 \delta_1 \delta_2}^{(\ell)} = \sum_{\ell_1, \ell_2=1}^{\ell} \sum_{\mu_1, \mu_2} \frac{d^2 z_{i_0; \delta_0}^{(\ell)}}{d\theta_{\mu_1}^{(\ell_1)} d\theta_{\mu_2}^{(\ell_2)}} \frac{dz_{i_1; \delta_1}^{(\ell)}}{d\theta_{\mu_1}^{(\ell_1)}} \frac{dz_{i_2; \delta_2}^{(\ell)}}{d\theta_{\mu_2}^{(\ell_2)}} \quad (30)$$

$$\widehat{\text{dd}_I \Theta}_{i_0 i_1 i_2 i_3; \delta_0 \delta_1 \delta_2 \delta_3}^{(\ell)} = \sum_{\ell_1, \ell_2, \ell_3=1}^{\ell} \sum_{\mu_1, \mu_2, \mu_3} \frac{d^3 z_{i_0; \delta_0}^{(\ell)}}{d\theta_{\mu_1}^{(\ell_1)} d\theta_{\mu_2}^{(\ell_2)} d\theta_{\mu_3}^{(\ell_3)}} \frac{dz_{i_1; \delta_1}^{(\ell)}}{d\theta_{\mu_1}^{(\ell_1)}} \frac{dz_{i_2; \delta_2}^{(\ell)}}{d\theta_{\mu_2}^{(\ell_2)}} \frac{dz_{i_3; \delta_3}^{(\ell)}}{d\theta_{\mu_3}^{(\ell_3)}} \quad (31)$$

$$\widehat{\text{dd}_{II} \Theta}_{i_1 i_2 i_3 i_4; \delta_1 \delta_2 \delta_3 \delta_4}^{(\ell)} = \sum_{\ell_1, \ell_2, \ell_3=1}^{\ell} \sum_{\mu_1, \mu_2, \mu_3} \frac{d^2 z_{i_1; \delta_1}^{(\ell)}}{d\theta_{\mu_1}^{(\ell_1)} d\theta_{\mu_3}^{(\ell_3)}} \frac{d^2 z_{i_2; \delta_2}^{(\ell)}}{d\theta_{\mu_2}^{(\ell_2)} d\theta_{\mu_3}^{(\ell_3)}} \frac{dz_{i_3; \delta_3}^{(\ell)}}{d\theta_{\mu_1}^{(\ell_1)}} \frac{dz_{i_4; \delta_4}^{(\ell)}}{d\theta_{\mu_2}^{(\ell_2)}}. \quad (32)$$

Their the definitions of their cumulants define the tensors P, Q, R, S, T and U ,

$$\mathbb{E}_{\theta}^c \left[\widehat{\text{d}\Theta}_{i_0 i_1 i_2; \delta_0 \delta_1 \delta_2}^{(\ell)}, z_{i_3; \delta_3}^{(\ell)} \right] = \frac{1}{n_{\ell-1}} \left[\delta_{i_0 i_3} \delta_{i_1 i_2} P_{\delta_0 \delta_1 \delta_2 \delta_3}^{(\ell)} + \delta_{i_0 i_1} \delta_{i_2 i_3} Q_{\delta_0 \delta_5 \delta_6 \delta_7}^{(\ell)} + \delta_{i_0 i_2} \delta_{i_1 i_3} Q_{\delta_0 \delta_2 \delta_1 \delta_3}^{(\ell)} \right] \quad (33)$$

$$\mathbb{E}_{\theta}^c \left[\widehat{\text{dd}_I \Theta}_{i_0 i_1 i_2 i_3; \delta_0 \delta_1 \delta_2 \delta_3}^{(\ell)} \right] = \frac{1}{n_{\ell-1}} \left[\delta_{i_0 i_1} \delta_{i_2 i_3} R_{\delta_0 \delta_1 \delta_2 \delta_3}^{(\ell)} + \delta_{i_0 i_2} \delta_{i_3 i_1} R_{\delta_0 \delta_2 \delta_3 \delta_1}^{(\ell)} + \delta_{i_0 i_3} \delta_{i_1 i_2} R_{\delta_0 \delta_3 \delta_1 \delta_2}^{(\ell)} \right] \quad (34)$$

$$\mathbb{E}_{\theta}^c \left[\widehat{\text{dd}_{II} \Theta}_{i_1 i_2 i_3 i_4; \delta_1 \delta_2 \delta_3 \delta_4}^{(\ell)} \right] = \frac{1}{n_{\ell-1}} \left[\delta_{i_1 i_2} \delta_{i_3 i_4} S_{\delta_1 \delta_2 \delta_3 \delta_4}^{(\ell)} + \delta_{i_1 i_3} \delta_{i_4 i_2} T_{\delta_1 \delta_3 \delta_4 \delta_2}^{(\ell)} + \delta_{i_1 i_4} \delta_{i_2 i_3} U_{\delta_1 \delta_4 \delta_2 \delta_3}^{(\ell)} \right]. \quad (35)$$

C Feynman rules

In this appendix, we provide the complete list of Feynman rules, including those described in the summary in Section 4.1 above.

- (i) External vertices (which correspond to the quantities which appear in the expectation value) are represented by filled dots.

- (a) *Solid external lines* represent preactivations [18]

$$z_{\alpha} \equiv \alpha \bullet \text{---} \quad (36)$$

- (b) *Dotted external lines* represent NTK fluctuations

$$\widehat{\Delta \Theta}_{\alpha \beta} \equiv \begin{matrix} \beta \bullet \text{.....} \\ \alpha \bullet \text{.....} \end{matrix} \quad (37)$$

We will use different colors for external dotted lines corresponding to different NTKs.

- (c) dNTKs, $\widehat{\text{d}\Theta}_{\delta_0 \delta_1 \delta_2} = \sum_{\mu \nu} \frac{d^2 z_{\delta_0}}{d\theta_{\mu} d\theta_{\nu}} \frac{dz_{\delta_1}}{d\theta_{\mu}} \frac{dz_{\delta_2}}{d\theta_{\nu}}$ as defined in (30), are represented by one dotted double line and two dotted single lines. They carry the sample indices of the dNTK according to

$$\widehat{\text{d}\Theta}_{\delta_0 \delta_1 \delta_2} \equiv \begin{matrix} \delta_2 \bullet \text{.....} \\ \delta_1 \bullet \text{.....} \\ \delta_0 \bullet \text{.....} \end{matrix} \quad (38)$$

Here, the colors of the dotted lines again correspond to the θ in the definition of the dNTK. Since now, there are two different θ (the four θ appearing in the definition are contracted in pairs), there are two different colors. The double line corresponds to the second derivative, the two single lines correspond to the first derivatives. The colors indicate the contraction pattern between the θ .

- (d) The $\widehat{\text{dd}_I \Theta}_{\delta_0 \delta_1 \delta_2 \delta_3} = \sum_{\mu\nu\rho} \frac{d^3 z \delta_0}{d\theta_\mu d\theta_\nu d\theta_\rho} \frac{dz \delta_1}{d\theta_\mu} \frac{dz \delta_2}{d\theta_\nu} \frac{dz \delta_3}{d\theta_\rho}$, defined by (31) is represented by

$$\widehat{\text{dd}_I \Theta}_{\delta_0 \delta_1 \delta_2 \delta_3} \equiv \begin{array}{c} \delta_3 \text{ (green dotted)} \\ \delta_2 \text{ (blue dotted)} \\ \delta_1 \text{ (orange dotted)} \\ \delta_0 \text{ (pink triple)} \end{array} \quad (39)$$

As before, we use three colored dotted lines due to the presence of three types of θ . The triple line denotes the third derivative, and the three single lines represent the first derivatives. The colors indicate the contraction pattern among the θ .

- (e) $\widehat{\text{dd}_{II} \Theta}_{\delta_1 \delta_2 \delta_3 \delta_4} = \sum_{\mu\nu\rho} \frac{d^2 z \delta_1}{d\theta_\mu d\theta_\nu} \frac{d^2 z \delta_2}{d\theta_\mu d\theta_\nu} \frac{dz \delta_3}{d\theta_\mu} \frac{dz \delta_4}{d\theta_\nu}$, as defined in (32), are denoted by

$$\widehat{\text{dd}_{II} \Theta}_{\delta_1 \delta_2 \delta_3 \delta_4} \equiv \begin{array}{c} \delta_4 \text{ (orange double)} \\ \delta_3 \text{ (blue double)} \\ \delta_2 \text{ (grey double)} \\ \delta_1 \text{ (red double)} \end{array} \quad (40)$$

Here we use again three colored lines for the three types of θ . The two double lines correspond to the second derivatives, and the two single lines represent the first derivatives. The colors indicate the contraction pattern among the θ .

- (ii) The external lines are attached to *cubic vertices*, which are vertices connected to two external lines and one *internal line*. Two external preactivations are joined in the vertex [18]

$$\begin{array}{c} \beta \\ \alpha \end{array} \begin{array}{c} \bullet \\ \bullet \end{array} \begin{array}{c} \diagup \\ \diagdown \end{array} \begin{array}{c} \widehat{\Delta G}_{i,\alpha\beta}^{(\ell)} \\ \text{wavy line} \end{array} \sim \frac{C_W^{(\ell+1)}}{n_\ell} \quad (41)$$

The line without dot is the internal line. We discuss its decoration in the next Feynman rule. For cubic interactions involving external NTK lines, we introduce the following Feynman rules

$$\begin{array}{ll} \begin{array}{c} \beta \\ \alpha \end{array} \begin{array}{c} \bullet \\ \bullet \end{array} \begin{array}{c} \diagup \\ \diagdown \end{array} \begin{array}{c} \widehat{\Delta \Omega}_{i,\alpha\beta}^{(\ell+1)} \\ \text{wavy line} \end{array} \sim \frac{1}{n_\ell} & \begin{array}{c} \beta \\ \alpha \end{array} \begin{array}{c} \bullet \\ \bullet \end{array} \begin{array}{c} \diagup \\ \diagdown \end{array} \begin{array}{c} \sigma_{i,\alpha}^{(\ell)} \sigma_{i,\beta}^{(\ell)} \\ \text{double line} \end{array} \sim \frac{C_W^{(\ell+1)}}{n_\ell} \\ \begin{array}{c} \beta \\ \alpha \end{array} \begin{array}{c} \bullet \\ \bullet \end{array} \begin{array}{c} \diagup \\ \diagdown \end{array} \begin{array}{c} \sigma_{i,\alpha}'^{(\ell)} \sigma_{i,\beta}'^{(\ell)} \\ \text{double line} \end{array} \sim \frac{C_W^{(\ell+1)}}{n_\ell} & \begin{array}{c} \beta \\ \alpha \end{array} \begin{array}{c} \bullet \\ \bullet \end{array} \begin{array}{c} \diagup \\ \diagdown \end{array} \begin{array}{c} \sigma_{i,\alpha}'^{(\ell)} \sigma_{i,\beta}'^{(\ell)} \\ \text{double line} \end{array} \sim \frac{C_W^{(\ell+1)}}{n_\ell} \end{array} \quad (42)$$

where $\widehat{\Delta \Omega}_{i,\alpha\beta}^{(\ell+1)} = \sigma_{i,\alpha}^{(\ell)} \sigma_{i,\beta}^{(\ell)} + C_W^{(\ell+1)} \Theta_{\alpha\beta}^{(\ell)} \sigma_{i,\alpha}'^{(\ell)} \sigma_{i,\beta}'^{(\ell)}$. For the remaining external lines due to the higher-derivative tensors, we introduce the following cubic vertices

$$\begin{array}{lll} \begin{array}{c} \beta \\ \alpha \end{array} \begin{array}{c} \bullet \\ \bullet \end{array} \begin{array}{c} \diagup \\ \diagdown \end{array} \begin{array}{c} \sigma_{i,\alpha}''^{(\ell)} \sigma_{i,\beta}^{(\ell)} \\ \text{double line} \end{array} \sim \frac{C_W^{(\ell+1)}}{n_\ell} & \begin{array}{c} \beta \\ \alpha \end{array} \begin{array}{c} \bullet \\ \bullet \end{array} \begin{array}{c} \diagup \\ \diagdown \end{array} \begin{array}{c} \sigma_{i,\alpha}'^{(\ell)} \sigma_{i,\beta}^{(\ell)} \\ \text{double line} \end{array} \sim \frac{C_W^{(\ell+1)}}{n_\ell} & \begin{array}{c} \beta \\ \alpha \end{array} \begin{array}{c} \bullet \\ \bullet \end{array} \begin{array}{c} \diagup \\ \diagdown \end{array} \begin{array}{c} \sigma_{i,\alpha}^{(\ell)} \sigma_{i,\beta}^{(\ell)} \\ \text{double line} \end{array} \sim \frac{1}{n_\ell} \\ \begin{array}{c} \beta \\ \alpha \end{array} \begin{array}{c} \bullet \\ \bullet \end{array} \begin{array}{c} \diagup \\ \diagdown \end{array} \begin{array}{c} \sigma_{i,\alpha}^{(\ell)} \sigma_{i,\alpha}''^{(\ell)} \sigma_{i,\beta}'^{(\ell)} \\ \text{triple line} \end{array} \sim \frac{C_W^{(\ell+1)}}{n_\ell} & \begin{array}{c} \beta \\ \alpha \end{array} \begin{array}{c} \bullet \\ \bullet \end{array} \begin{array}{c} \diagup \\ \diagdown \end{array} \begin{array}{c} \sigma_{i,\alpha}'^{(\ell)} \sigma_{i,\alpha}''^{(\ell)} \sigma_{i,\beta}'^{(\ell)} \\ \text{triple line} \end{array} \sim \frac{C_W^{(\ell+1)}}{n_\ell} & \begin{array}{c} \beta \\ \alpha \end{array} \begin{array}{c} \bullet \\ \bullet \end{array} \begin{array}{c} \diagup \\ \diagdown \end{array} \begin{array}{c} \sigma_{i,\alpha}''^{(\ell)} \sigma_{i,\alpha}'^{(\ell)} \sigma_{i,\beta}'^{(\ell)} \\ \text{triple line} \end{array} \sim \frac{C_W^{(\ell+1)}}{n_\ell} \\ \begin{array}{c} \beta \\ \alpha \end{array} \begin{array}{c} \bullet \\ \bullet \end{array} \begin{array}{c} \diagup \\ \diagdown \end{array} \begin{array}{c} \sigma_{i,\alpha}'^{(\ell)} \sigma_{i,\alpha}''^{(\ell)} \sigma_{i,\beta}'^{(\ell)} \\ \text{triple line} \end{array} \sim \frac{C_W^{(\ell+1)}}{n_\ell} & \begin{array}{c} \beta \\ \alpha \end{array} \begin{array}{c} \bullet \\ \bullet \end{array} \begin{array}{c} \diagup \\ \diagdown \end{array} \begin{array}{c} \sigma_{i,\alpha}^{(\ell)} \sigma_{i,\alpha}''^{(\ell)} \sigma_{i,\beta}'^{(\ell)} \\ \text{triple line} \end{array} \sim \frac{1}{n_\ell} & \begin{array}{c} \beta \\ \alpha \end{array} \begin{array}{c} \bullet \\ \bullet \end{array} \begin{array}{c} \diagup \\ \diagdown \end{array} \begin{array}{c} \Theta_{\alpha\beta}^{(\ell)} \sigma_{i,\alpha}''^{(\ell)} \sigma_{i,\beta}''^{(\ell)} \\ \text{triple line} \end{array} \sim \frac{C_W^{(\ell+1)}}{n_\ell} \end{array}$$

$$\begin{aligned}
& \text{Diagram 1: } \sim \frac{C_W^{(\ell+1)}}{n_\ell} \quad \text{Diagram 2: } \sim \frac{1}{n_\ell} \quad \text{Diagram 3: } \sim \frac{C_W^{(\ell+1)}}{n_\ell} \\
& \text{Diagram 4: } \sim \frac{1}{n_\ell} \quad \text{Diagram 5: } \sim \frac{C_W^{(\ell+1)}}{n_\ell}
\end{aligned} \tag{43}$$

- (iii) The internal lines from the vertices (42) are connected to a *propagator* which will be represented by a white blob

$$\langle \rangle_{K^{(\ell)}} \equiv \bigcirc \tag{44}$$

where $\langle \rangle_{K^{(\ell)}}$ stands for a Gaussian expectation value with mean zero and covariance given by the Gram matrix of the NNGP, as in (5). We take the expectation value over the decorations of the internal lines attached to the propagator, for instance

$$\widehat{\Delta\Omega_{i,\alpha\beta}} \bigcirc \widehat{\Delta\Omega_{i,\gamma\delta}} \sim \langle \widehat{\Delta\Omega_{i,\alpha\beta}} \widehat{\Delta\Omega_{i,\gamma\delta}} \rangle_{K^{(\ell)}}. \tag{45}$$

Propagators obey the following *selection rules*:

- (a) Propagators are only connected to internal lines emanating from the cubic vertices or the internal quartic vertices introduced below. In particular, propagators cannot be directly connected to other propagators.
 - (b) Dotted lines attached to a propagator do not appear in the Gaussian expectation value, since they are not decorated.
 - (c) Each preactivation line decorated with z_i acts as a derivative with respect to z_i on the argument of the Gaussian expectation value.
 - (d) The neural indices of all internal lines connected to the propagator have to be equal.
 - (e) If both dotted and dashed lines of the same color are connected to the propagator, these have to appear in pairs with the same sample index. The lines in a pair will be attached to different vertices. Furthermore, if both vertices connected with one color to the propagator are drawn in the orientation in which they are presented in the Feynman rules, the ordering from top to bottom of the sample indices (and therefore colors) of the lines connected to both vertices have to be the same.
 - (f) Pairs of dashed lines of the same color connected to the propagator add a factor of $\Theta_{\alpha\beta}$ if they are connected to different vertices. Here, α and β are the sample indices of the two lines in the pair.
- (iv) The 10 rank-four tensors into which we decompose the cumulants will be represented by *quartic interactions* with four external lines. For preactivations, we use the vertex V_4 [18]

$$\frac{1}{n_\ell} V_{1234}^{(\ell+1)} \tag{46}$$

We introduce the following quartic vertices containing NTK and preactivation lines

$$\begin{aligned}
& \text{Diagram D: } \frac{1}{n_\ell} D_{\alpha_1 \alpha_2 \alpha_3 \alpha_4}^{(\ell+1)} \quad \text{Diagram F: } \frac{1}{n_\ell} F_{\alpha_1 \alpha_3 \alpha_2 \alpha_4}^{(\ell+1)} \quad \text{Diagram A: } \frac{1}{n_\ell} A_{\alpha_1 \alpha_2 \alpha_3 \alpha_4}^{(\ell+1)} \quad \text{Diagram B: } \frac{1}{n_\ell} B_{\alpha_1 \alpha_3 \alpha_2 \alpha_4}^{(\ell+1)}
\end{aligned} \tag{47}$$

For the higher-derivative tensors, we introduce

$$\begin{aligned}
& \frac{1}{n_\ell} P_{\alpha_3 \alpha_1 \alpha_2 \alpha_4}^{(\ell+1)} & \frac{1}{n_\ell} Q_{\alpha_1 \alpha_2 \alpha_3 \alpha_4}^{(\ell+1)} & \frac{1}{n_\ell} R_{\alpha_1 \alpha_2 \alpha_3 \alpha_4}^{(\ell+1)} \\
& \frac{1}{n_\ell} S_{\alpha_1 \alpha_2 \alpha_3 \alpha_4}^{(\ell+1)} & \frac{1}{n_\ell} T_{\alpha_1 \alpha_3 \alpha_4 \alpha_2}^{(\ell+1)} & \frac{1}{n_\ell} U_{\alpha_1 \alpha_4 \alpha_2 \alpha_3}^{(\ell+1)}
\end{aligned} \tag{48}$$

The quartic vertices can also appear with four internal lines instead. In this case, they correspond to tensors in layer ℓ instead of $\ell+1$ and are connected to propagators. Further quartic tensors for the remaining tensors involving preactivations, the dNTK and ddNTK are introduced in Appendix B. For the mean NNGP and NTK corrections $K^{\{1\}}$ and $\Theta^{\{1\}}$, we similarly introduce *quadratic vertices* of valence two.

- (v) Internal lines attached to cubic or internal quartic vertices have unassigned neural indices (e.g. i in the vertices in (42)). Similarly, internal (solid) preactivation lines have unassigned sample indices. To assemble the term corresponding to a certain diagram, multiply the expressions corresponding to vertices and propagators and sum over all unassigned neural and sample indices. The complete expression for a cumulant is given by summing over all Feynman diagrams with the correct external lines and order in $1/n$.

D Feynman diagrams

In this Appendix, we provide the formal definition of the relevant tensors describing the statistics of the NTK, dNTK and ddNTKS at leading order in $\frac{1}{n}$, as well as their diagrammatic representation and corresponding algebraic expressions.

D.1 NTK-Preactivation cross correlator

As discussed in section 3, the first non-trivial correlator involving preactivations and the NTK can be written as

$$\begin{aligned}
& \mathbb{E}_\theta^c [z_{i_1}^{(\ell+1)}(x_1), z_{i_2}^{(\ell+1)}(x_2), \widehat{\Delta\Theta}_{i_3 i_4}^{(\ell+1)}(x_3, x_4)] \\
& = \frac{1}{n_\ell} \left(D_{1234}^{(\ell+1)} \delta_{i_1 i_2} \delta_{i_3 i_4} + F_{1324}^{(\ell+1)} \delta_{i_1 i_3} \delta_{i_2 i_4} + F_{1423}^{(\ell+1)} \delta_{i_1 i_4} \delta_{i_2 i_3} \right).
\end{aligned} \tag{49}$$

The Feynman rules we studied in the main text then allow us to write the following diagrams for the tensor $D_{1234}^{(\ell+1)}$:

$$\frac{1}{n_\ell} D_{1234}^{(\ell+1)} = \sum_j \text{diagram 1} + \sum_{j_1, j_2} \text{diagram 2}$$

$$+ \sum_{j_1, j_2} \text{Diagram} \quad (50)$$

whose algebraic representation reads

$$\begin{aligned} \frac{1}{n_\ell} D_{1234}^{(\ell+1)} &= \frac{C_W^{(\ell+1)}}{n_\ell} \langle \widehat{\Delta G}_{12}^{(\ell)} \widehat{\Delta \Omega}_{34}^{(\ell+1)} \rangle_{K^{(\ell)}} \\ &+ \frac{C_W^{(\ell+1)}}{4n_{\ell-1}} \sum_{\beta_1, \beta_2, \beta_3, \beta_4 \in \{1, 2, 3, 4\}} V_{(\beta_1 \beta_2)(\beta_3 \beta_4)}^{(\ell)} \langle \frac{d^2(\widehat{\Delta G}_{12}^{(\ell)})}{dz_{\beta_1}^{(\ell)} dz_{\beta_2}^{(\ell)}} \rangle_{K^{(\ell)}} \langle \frac{d^2(\widehat{\Delta \Omega}_{34}^{(\ell+1)})}{dz_{\beta_1}^{(\ell)} dz_{\beta_2}^{(\ell)}} \rangle_{K^{(\ell)}} \\ &+ \frac{(C_W^{(\ell+1)})^2}{2n_{\ell-1}} \sum_{\beta_1, \beta_2 \in \{1, 2, 3, 4\}} \langle \frac{d^2(\widehat{\Delta G}_{12}^{(\ell)})}{dz_{\beta_1}^{(\ell)} dz_{\beta_2}^{(\ell)}} \rangle_{K^{(\ell)}} \langle \sigma_3'^{(\ell)} \sigma_4'^{(\ell)} \rangle_{K^{(\ell)}} D_{\beta_1 \beta_2 34}^{(\ell)} \end{aligned} \quad (51)$$

The tensor $F^{(\ell+1)}$ was studied in detail in the main text, thus we omit its discussion.

D.2 NTK variance

As shown in [17], the NTK variance can be written in the compact form

$$\begin{aligned} \mathbb{E}_\theta^c[\widehat{\Delta \Theta}_{i_1 i_2}^{(\ell+1)}(x_1, x_2), \widehat{\Delta \Theta}_{i_3 i_4}^{(\ell+1)}(x_3, x_4)] \\ = \frac{1}{n_\ell} (A_{1234}^{(\ell+1)} \delta_{i_1 i_2} \delta_{i_3 i_4} + B_{1324}^{(\ell+1)} \delta_{i_1 i_3} \delta_{i_2 i_4} + B_{1423}^{(\ell+1)} \delta_{i_1 i_4} \delta_{i_2 i_3}) . \end{aligned} \quad (52)$$

The use of the NTK Feynman rules of section 4, then simply dictate the definition of the tensor $A_{1234}^{(\ell+1)}$:

$$\text{Diagram} = \sum_j \text{Diagram} + \sum_{j_1, j_2} \text{Diagram} + \sum_{j_1, j_2} \text{Diagram} + \sum_{j_1, j_2} \text{Diagram} \quad (53)$$

which translates into the analytical expression

$$\frac{1}{n_\ell} A_{1234}^{(\ell+1)} = \frac{1}{n_\ell} \langle \widehat{\Delta \Omega}_{12}^{(\ell+1)} \widehat{\Delta \Omega}_{34}^{(\ell+1)} \rangle_{K^{(\ell)}}$$

$$\begin{aligned}
& + \frac{1}{4n_{\ell-1}} \sum_{\beta_1, \beta_2, \beta_3, \beta_4 \in \{1,2,3,4\}} V_{(\beta_1\beta_2)(\beta_3\beta_4)}^{(\ell)} \left\langle \frac{d^2(\widehat{\Delta\Omega}_{12}^{(\ell+1)})}{dz_{\beta_1}^{(\ell)} dz_{\beta_2}^{(\ell)}} \right\rangle_{K^{(\ell)}} \left\langle \frac{d^2(\widehat{\Delta\Omega}_{34}^{(\ell+1)})}{dz_{\beta_1}^{(\ell)} dz_{\beta_2}^{(\ell)}} \right\rangle_{K^{(\ell)}} \\
& + \frac{C_W^{(\ell+1)}}{2n_{\ell-1}} \sum_{\beta_1, \beta_2 \in \{1,2,3,4\}} \left\langle \frac{d^2(\widehat{\Delta\Omega}_{12}^{(\ell+1)})}{dz_{\beta_1}^{(\ell)} dz_{\beta_2}^{(\ell)}} \right\rangle_{K^{(\ell)}} \langle \sigma_3'^{(\ell)} \sigma_4'^{(\ell)} \rangle_{K^{(\ell)}} D_{\beta_1\beta_2 34}^{(\ell)} \\
& + \frac{C_W^{(\ell+1)}}{2n_{\ell-1}} \sum_{\beta_3, \beta_4 \in \{1,2,3,4\}} \left\langle \frac{d^2(\widehat{\Delta\Omega}_{34}^{(\ell+1)})}{dz_{\beta_3}^{(\ell)} dz_{\beta_4}^{(\ell)}} \right\rangle_{K^{(\ell)}} \langle \sigma_1'^{(\ell)} \sigma_2'^{(\ell)} \rangle_{K^{(\ell)}} D_{12\beta_3\beta_4}^{(\ell)} \\
& + \frac{(C_W^{(\ell+1)})^2}{n_{\ell-1}} \langle \sigma_1'^{(\ell)} \sigma_2'^{(\ell)} \rangle_{K^{(\ell)}} \langle \sigma_3'^{(\ell)} \sigma_4'^{(\ell)} \rangle_{K^{(\ell)}} A_{1234}^{(\ell)}
\end{aligned} \tag{54}$$

Similarly, one can find the tensor $B^{(\ell+1)}$ from the following diagrammatic relation:

$$\frac{1}{n_\ell} B_{1324}^{(\ell+1)} = \sum_j \text{diagram} + \sum_{j_1, j_2} \text{diagram} \tag{55}$$

whose algebraic interpretation reads

$$\begin{aligned}
\frac{1}{n_\ell} B_{1324}^{(\ell+1)} &= \frac{(C_W^{(\ell+1)})^2}{n_\ell} \Theta_{12}^{(\ell)} \Theta_{34}^{(\ell)} \langle \sigma_1'^{(\ell)} \sigma_2'^{(\ell)} \sigma_3'^{(\ell)} \sigma_4'^{(\ell)} \rangle_{K^{(\ell)}} \\
&+ \frac{(C_W^{(\ell+1)})^2}{n_{\ell-1}} \langle \sigma_1'^{(\ell)} \sigma_3'^{(\ell)} \rangle_{K^{(\ell)}} \langle \sigma_2'^{(\ell)} \sigma_4'^{(\ell)} \rangle_{K^{(\ell)}} B_{1324}^{(\ell)}
\end{aligned} \tag{56}$$

D.3 dNTK-Preactivation cross correlator

The first relevant correlator at leading order in $\frac{1}{n}$ including the dNTK is given by [17]

$$\mathbb{E}_\theta \left[\widehat{d\Theta}_{i_0 i_1 i_2}^{(\ell+1)}(x_0, x_1, x_2), z_{i_3}^{(\ell+1)}(x_3) \right] = \frac{1}{n_\ell} \left[\delta_{i_0 i_3} \delta_{i_1 i_2} P_{0123}^{(\ell+1)} + \delta_{i_0 i_1} \delta_{i_2 i_3} Q_{0123}^{(\ell+1)} + \delta_{i_0 i_2} \delta_{i_1 i_3} Q_{0213}^{(\ell+1)} \right] \tag{57}$$

The Feynman rules introduced in Appendix C, then lead to the following expression for the tensor $P_{0123}^{(\ell+1)}$:

$$\frac{1}{n_\ell} P_{0123}^{(\ell+1)} = \sum_j \text{diagram} + \sum_{j_1, j_2} \text{diagram} + \sum_{j_1, j_2} \text{diagram} \tag{58}$$

or, equivalently

$$\frac{1}{n_\ell} P_{0123}^{(\ell+1)} = \frac{(C_W^{(\ell+1)})^2}{n_\ell} \Theta_{01}^{(\ell)} \Theta_{02}^{(\ell)} \langle \sigma_1'^{(\ell)} \sigma_2'^{(\ell)} \sigma_0''^{(\ell)} \sigma_3^{(\ell)} \rangle_{K^{(\ell)}}$$

$$\begin{aligned}
& + \frac{(C_W^{(\ell+1)})^2}{n_{\ell-1}} \langle \sigma_1'^{(\ell)} \sigma_2'^{(\ell)} \rangle_{K^{(\ell)}} \langle \sigma_0''^{(\ell)} \sigma_0^{(\ell)} \rangle_{K^{(\ell)}} B_{0012}^{(\ell)} \\
& + \frac{(C_W^{(\ell+1)})^2}{n_{\ell-1}} \langle \sigma_1'^{(\ell)} \sigma_2'^{(\ell)} \rangle_{K^{(\ell)}} \sum_{\beta_3 \in \{1,2,3,4\}} \langle \frac{d(\sigma_0'^{(\ell)} \sigma_3^{(\ell)})}{dz_{\beta_3}^{(\ell)}} \rangle_{K^{(\ell)}} P_{012\beta_3}^{(\ell)}
\end{aligned} \tag{59}$$

The application of these same rules to the construction of the tensor $Q_{0123}^{(\ell+1)}$ yields:

$$\begin{aligned}
& \frac{1}{n_\ell} Q_{0123}^{(\ell+1)} = \frac{1}{C_W^{(\ell+1)}} \frac{1}{n_\ell} F_{0123}^{(\ell+1)} + \sum_j \frac{1}{n_\ell} F_{0123}^{(\ell+1)} + \sum_j \frac{1}{n_\ell} F_{0123}^{(\ell+1)} \\
& + \sum_{j_1, j_2} \frac{1}{n_{\ell-1}} F_4^{(\ell)} + \sum_{j_1, j_2} \frac{1}{n_{\ell-1}} Q_4^{(\ell)}
\end{aligned} \tag{60}$$

which, in algebraic notation, reads

$$\begin{aligned}
\frac{1}{n_\ell} Q_{0123}^{(\ell+1)} &= \frac{1}{C_W^{(\ell+1)} n_\ell} F_{0123}^{(\ell+1)} + \frac{(C_W^{(\ell+1)})^2}{n_\ell} \Theta_{01}^{(\ell)} \Theta_{02}^{(\ell)} \langle \sigma_0''^{(\ell)} \sigma_1'^{(\ell)} \sigma_2'^{(\ell)} \sigma_3^{(\ell)} \rangle_{K^{(\ell)}} \\
& + \frac{(C_W^{(\ell+1)})^2}{n_{\ell-1}} \Theta_{01}^{(\ell)} \sum_{\lambda_1, \lambda_3 \in \{0,1,2,3\}} \langle \frac{d(\sigma_0''^{(\ell)} \sigma_1'^{(\ell)})}{dz_{\lambda_1}^{(\ell)}} \rangle_{K^{(\ell)}} \langle \frac{d(\sigma_2'^{(\ell)} \sigma_3^{(\ell)})}{dz_{\lambda_3}^{(\ell)}} \rangle_{K^{(\ell)}} F_{\lambda_1 0 \lambda_3 2}^{(\ell)} \\
& + \frac{(C_W^{(\ell+1)})^2}{n_{\ell-1}} \langle \sigma_0'^{(\ell)} \sigma_1'^{(\ell)} \rangle_{K^{(\ell)}} \sum_{\beta_3 \in \{0,1,2,3\}} \langle \frac{d(\sigma_2'^{(\ell)} \sigma_3^{(\ell)})}{dz_{\beta_3}^{(\ell)}} \rangle_{K^{(\ell)}} Q_{012\beta_3}^{(\ell)}
\end{aligned} \tag{61}$$

D.4 dd_INTK mean

Unlike the previous cases, the first non-trivial correlator containing the ddNTK is its mean itself. For the first type, one finds that [17]:

$$\mathbb{E}_\theta^c \left[\widehat{\text{dd}_I \Theta}_{i_0 i_1 i_2 i_3}^{(\ell+1)}(x_0, x_1, x_2, x_3) \right] = \frac{1}{n_\ell} \left[\delta_{i_0 i_1} \delta_{i_2 i_3} R_{0123}^{(\ell+1)} + \delta_{i_0 i_2} \delta_{i_3 i_1} R_{0213}^{(\ell+1)} + \delta_{i_0 i_3} \delta_{i_1 i_2} R_{0312}^{(\ell+1)} \right] \tag{62}$$

Again, the use of the Feynman rules C, imply the following structure for the tensor $R_{0123}^{(\ell+1)}$:

$$\frac{1}{n_\ell} R_{0123}^{(\ell+1)} = \sum_j \frac{1}{n_\ell} R_{0123}^{(\ell+1)} + \sum_{j_1, j_2} \frac{1}{n_{\ell-1}} B_4^{(\ell)}$$

$$\begin{aligned}
& + \sum_{j_1, j_2} \text{Diagram 1} \\
& + \sum_j \text{Diagram 2} + \sum_{j_1, j_2} \text{Diagram 3} \\
& + \sum_{j_1, j_2} \text{Diagram 4}
\end{aligned} \tag{63}$$

or, in analytical form

$$\begin{aligned}
\frac{1}{n_\ell} R_{0123}^{(\ell+1)} &= \frac{C_W^{(\ell+1)}}{n_\ell} \Theta_{02}^{(\ell)} \Theta_{03}^{(\ell)} \langle \sigma_0''^{(\ell)} \sigma_1^{(\ell)} \sigma_2'^{(\ell)} \sigma_3'^{(\ell)} \rangle_{K^{(\ell)}} + \frac{C_W^{(\ell+1)}}{n_{\ell-1}} \langle \sigma_0''^{(\ell)} \sigma_1^{(\ell)} \rangle_{K^{(\ell)}} \langle \sigma_2'^{(\ell)} \sigma_3'^{(\ell)} \rangle_{K^{(\ell)}} B_{0023}^{(\ell)} \\
&+ \frac{C_W^{(\ell+1)}}{n_{\ell-1}} \langle \sigma_2'^{(\ell)} \sigma_3'^{(\ell)} \rangle_{K^{(\ell)}} \sum_{\lambda_1 \in \{0,1,2,3\}} \langle \frac{d(\sigma_0''^{(\ell)} \sigma_1^{(\ell)})}{dz_{\lambda_1}^{(\ell)}} \rangle_{K^{(\ell)}} P_{023\lambda_1}^{(\ell)} \\
&+ \frac{(C_W^{(\ell+1)})^2}{n_\ell} \Theta_{01}^{(\ell)} \Theta_{02}^{(\ell)} \Theta_{03}^{(\ell)} \langle \sigma_0'''^{(\ell)} \sigma_1^{(\ell)} \sigma_2'^{(\ell)} \sigma_3'^{(\ell)} \rangle_{K^{(\ell)}} \\
&+ \frac{(C_W^{(\ell+1)})^2}{n_{\ell-1}} \Theta_{01}^{(\ell)} \langle \sigma_0'''^{(\ell)} \sigma_1^{(\ell)} \rangle_{K^{(\ell)}} \langle \sigma_2'^{(\ell)} \sigma_3'^{(\ell)} \rangle_{K^{(\ell)}} B_{0023}^{(\ell)} \\
&+ \frac{(C_W^{(\ell+1)})^2}{n_{\ell-1}} \Theta_{01}^{(\ell)} \langle \sigma_2'^{(\ell)} \sigma_3'^{(\ell)} \rangle_{K^{(\ell)}} \sum_{\lambda_1 \in \{0,1,2,3\}} \langle \frac{d(\sigma_0''^{(\ell)} \sigma_1^{(\ell)})}{dz_{\lambda_1}^{(\ell)}} \rangle_{K^{(\ell)}} P_{023\lambda_1}^{(\ell)} \\
&+ \frac{(C_W^{(\ell+1)})^2}{n_{\ell-1}} \langle \sigma_0'^{(\ell)} \sigma_1'^{(\ell)} \rangle_{K^{(\ell)}} \langle \sigma_2'^{(\ell)} \sigma_3'^{(\ell)} \rangle_{K^{(\ell)}} R_{0123}^{(\ell)}
\end{aligned} \tag{64}$$

D.5 dd_{II}NTK mean

Analogously, the mean of the second type of the ddNTK can be shown to have the structure [17]:

$$\mathbb{E}_\theta^c \left[\widehat{\text{dd}_{\text{II}} \Theta}_{i_0 i_1 i_2 i_3}^{(\ell+1)}(x_1 x_2 x_3 x_4) \right] = \frac{1}{n_\ell} \left[\delta_{i_1 i_2} \delta_{i_3 i_4} S_{1234}^{(\ell+1)} + \delta_{i_1 i_3} \delta_{i_2 i_4} T_{1324}^{(\ell+1)} + \delta_{i_1 i_4} \delta_{i_2 i_3} U_{1423}^{(\ell+1)} \right] \tag{65}$$

Once more, the set of Feynman rules **C** dictates the definition of the tensors on the r.h.s of (65). For the

tensor $S_{1234}^{(\ell+1)}$, one finds

$$\begin{aligned}
\frac{1}{n_\ell} S_{1234}^{(\ell+1)} &= \sum_j \text{diagram} + \sum_{j_1, j_2} \text{diagram} + \sum_j \text{diagram} + \sum_{j_1, j_2} \text{diagram} \\
&\quad + \sum_{j_1, j_2} \text{diagram}
\end{aligned} \tag{66}$$

or, in algebraic form

$$\begin{aligned}
\frac{1}{n_\ell} S_{1234}^{(\ell+1)} &= \frac{C_W^{(\ell+1)}}{n_\ell} \langle \sigma_1^{(\ell)} \sigma_2^{(\ell)} \sigma_3^{(\ell)} \sigma_4^{(\ell)} \rangle_{K^{(\ell)}} \Theta_{13}^{(\ell)} \Theta_{24}^{(\ell)} + \frac{C_W^{(\ell+1)}}{n_{\ell-1}} \langle \sigma_1^{(\ell)} \sigma_2^{(\ell)} \rangle_{K^{(\ell)}} \langle \sigma_3^{(\ell)} \sigma_4^{(\ell)} \rangle_{K^{(\ell)}} B_{1234}^{(\ell)} \\
&\quad + \frac{(C_W^{(\ell+1)})^2}{n_{\ell-1}} \Theta_{12}^{(\ell)} \Theta_{13}^{(\ell)} \Theta_{24}^{(\ell)} \langle \sigma_1^{(\ell)} \sigma_2^{(\ell)} \sigma_3^{(\ell)} \sigma_4^{(\ell)} \rangle_{K^{(\ell)}} \\
&\quad + \frac{(C_W^{(\ell+1)})^2}{n_{\ell-1}} \Theta_{12}^{(\ell)} \langle \sigma_1^{(\ell)} \sigma_2^{(\ell)} \rangle_{K^{(\ell)}} \langle \sigma_3^{(\ell)} \sigma_4^{(\ell)} \rangle_{K^{(\ell)}} B_{1234}^{(\ell)} \\
&\quad + \frac{(C_W^{(\ell+1)})^2}{n_{\ell-1}} \langle \sigma_1^{(\ell)} \sigma_2^{(\ell)} \rangle_{K^{(\ell)}} \langle \sigma_3^{(\ell)} \sigma_4^{(\ell)} \rangle_{K^{(\ell)}} S_{1234}^{(\ell)}
\end{aligned} \tag{67}$$

For the tensor $T_{1324}^{(\ell+1)}$, one obtains

$$\begin{aligned}
\frac{1}{n_\ell} T_{1324}^{(\ell+1)} &= \sum_j \text{diagram} + \sum_{j_1, j_2} \text{diagram} + \sum_j \text{diagram} + \sum_{j_1, j_2} \text{diagram} \\
&\quad + \sum_{j_1, j_2} \text{diagram} + \sum_j \text{diagram} + \sum_{j_1, j_2} \text{diagram} + \sum_j \text{diagram}
\end{aligned}$$

$$\begin{aligned}
& + \sum_{j_1, j_2} \text{Diagram 1} \\
& + \sum_j \text{Diagram 2} + \sum_{j_1, j_2} \text{Diagram 3} \\
& + \sum_{j_1, j_2} \text{Diagram 4} \\
& + \sum_{j_1, j_2} \text{Diagram 5}
\end{aligned} \tag{68}$$

with algebraic representation given by

$$\begin{aligned}
\frac{1}{n_{\ell}} T_{1324}^{(\ell+1)} &= \frac{1}{n_{\ell}} \langle \sigma_1^{(\ell)} \sigma_3^{(\ell)} \sigma_2^{\prime(\ell)} \sigma_4^{(\ell)} \rangle_{K^{(\ell)}} \Theta_{12}^{(\ell)} \\
&+ \frac{1}{n_{\ell-1}} \sum_{\lambda_3, \lambda_4 \in \{1, 2, 3, 4\}} \langle \frac{d(\sigma_1^{(\ell)} \sigma_3^{(\ell)})}{dz_{\lambda_3}^{(\ell)}} \rangle_{K^{(\ell)}} \langle \frac{d(\sigma_2^{(\ell)} \sigma_4^{(\ell)})}{dz_{\lambda_4}^{(\ell)}} \rangle_{K^{(\ell)}} F_{\lambda_3 1 \lambda_4 2}^{(\ell)} \\
&+ \frac{C_W^{(\ell+1)}}{n_{\ell}} \Theta_{12}^{(\ell)} \Theta_{24}^{(\ell)} \langle \sigma_1^{(\ell)} \sigma_3^{(\ell)} \sigma_2^{\prime(\ell)} \sigma_4^{\prime(\ell)} \rangle_{K^{(\ell)}} \\
&+ \frac{C_W^{(\ell+1)}}{n_{\ell-1}} \Theta_{24}^{(\ell)} \sum_{\lambda_3, \lambda_4 \in \{1, 2, 3, 4\}} \langle \frac{d(\sigma_1^{(\ell)} \sigma_3^{(\ell)})}{dz_{\lambda_3}^{(\ell)}} \rangle_{K^{(\ell)}} \langle \frac{d(\sigma_2^{\prime(\ell)} \sigma_4^{(\ell)})}{dz_{\lambda_4}^{(\ell)}} \rangle_{K^{(\ell)}} F_{\lambda_3 1 \lambda_4 2}^{(\ell)} \\
&+ \frac{C_W^{(\ell+1)}}{n_{\ell-1}} \langle \sigma_2^{(\ell)} \sigma_4^{(\ell)} \rangle_{K^{(\ell)}} \sum_{\lambda_3 \in \{1, 2, 3, 4\}} \langle \frac{d(\sigma_1^{(\ell)} \sigma_3^{\prime(\ell)})}{dz_{\lambda_3}^{(\ell)}} \rangle_{K^{(\ell)}} Q_{241 \lambda_3}^{(\ell)} \\
&+ \frac{C_W^{(\ell+1)}}{n_{\ell}} \Theta_{12}^{(\ell)} \Theta_{13}^{(\ell)} \langle \sigma_1^{\prime(\ell)} \sigma_3^{(\ell)} \sigma_2^{\prime(\ell)} \sigma_4^{(\ell)} \rangle_{K^{(\ell)}} \\
&+ \frac{C_W^{(\ell+1)}}{n_{\ell-1}} \Theta_{13}^{(\ell)} \sum_{\lambda_3, \lambda_4 \in \{1, 2, 3, 4\}} \langle \frac{d(\sigma_1^{\prime(\ell)} \sigma_3^{(\ell)})}{dz_{\lambda_3}^{(\ell)}} \rangle_{K^{(\ell)}} \langle \frac{d(\sigma_2^{(\ell)} \sigma_4^{(\ell)})}{dz_{\lambda_4}^{(\ell)}} \rangle_{K^{(\ell)}} F_{\lambda_4 2 \lambda_3 1}^{(\ell)} \\
&+ \frac{C_W^{(\ell+1)}}{n_{\ell-1}} \langle \sigma_1^{(\ell)} \sigma_3^{\prime(\ell)} \rangle_{K^{(\ell)}} \sum_{\lambda_4 \in \{1, 2, 3, 4\}} \langle \frac{d(\sigma_2^{(\ell)} \sigma_4^{\prime(\ell)})}{dz_{\lambda_4}^{(\ell)}} \rangle_{K^{(\ell)}} Q_{132 \lambda_4}^{(\ell)} \\
&+ \frac{(C_W^{(\ell+1)})^2}{n_{\ell}} \Theta_{13}^{(\ell)} \Theta_{24}^{(\ell)} \Theta_{12}^{(\ell)} \langle \sigma_1^{\prime(\ell)} \sigma_3^{(\ell)} \sigma_2^{\prime(\ell)} \sigma_4^{\prime(\ell)} \rangle_{K^{(\ell)}}
\end{aligned}$$

$$\begin{aligned}
& + \frac{(C_W^{\ell+1})^2}{n_{\ell-1}} \Theta_{13}^{(\ell)} \Theta_{24}^{(\ell)} \sum_{\lambda_3, \lambda_4 \in \{1,2,3,4\}} \left\langle \frac{d(\sigma_1''^{(\ell)} \sigma_3'^{(\ell)})}{dz_{\lambda_3}^{(\ell)}} \right\rangle_{K^{(\ell)}} \left\langle \frac{d(\sigma_2''^{(\ell)} \sigma_4'^{(\ell)})}{dz_{\lambda_4}^{(\ell)}} \right\rangle_{K^{(\ell)}} F_{\lambda_3 1 \lambda_4 2}^{(\ell)} \\
& + \frac{(C_W^{\ell+1})^2}{n_{\ell-1}} \Theta_{13}^{(\ell)} \langle \sigma_2'^{(\ell)} \sigma_4'^{(\ell)} \rangle_{K^{(\ell)}} \sum_{\lambda_3 \in \{1,2,3,4\}} \left\langle \frac{d(\sigma_1''^{(\ell)} \sigma_3'^{(\ell)})}{dz_{\lambda_3}^{(\ell)}} \right\rangle_{K^{(\ell)}} \mathcal{Q}_{241\lambda_3}^{(\ell)} \\
& + \frac{(C_W^{\ell+1})^2}{n_{\ell-1}} \Theta_{24}^{(\ell)} \langle \sigma_1'^{(\ell)} \sigma_3'^{(\ell)} \rangle_{K^{(\ell)}} \sum_{\lambda_4 \in \{1,2,3,4\}} \left\langle \frac{d(\sigma_2''^{(\ell)} \sigma_4'^{(\ell)})}{dz_{\lambda_4}^{(\ell)}} \right\rangle_{K^{(\ell)}} \mathcal{Q}_{132\lambda_4}^{(\ell)} \\
& + \frac{(C_W^{\ell+1})^2}{n_{\ell-1}} \langle \sigma_1'^{(\ell)} \sigma_3'^{(\ell)} \rangle_{K^{(\ell)}} \langle \sigma_2'^{(\ell)} \sigma_4'^{(\ell)} \rangle_{K^{(\ell)}} T_{1324}^{(\ell)}
\end{aligned} \tag{69}$$

Finally, for the tensor $U_{1423}^{(\ell+1)}$, one learns

$$\begin{aligned}
\frac{1}{n_\ell} U_{1423}^{(\ell+1)} &= \sum_j \text{Diagram 1} + \sum_{j_1, j_2} \text{Diagram 2} \\
&= \sum_j \left(\text{Diagram 1} \right) + \sum_{j_1, j_2} \left(\text{Diagram 2} \right)
\end{aligned} \tag{70}$$

whose analytical expression reads

$$\begin{aligned}
\frac{1}{n_\ell} U_{1423}^{(\ell+1)} &= \frac{(C_W^{\ell+1})^2}{n_\ell} \Theta_{12}^{(\ell)} \Theta_{24}^{(\ell)} \Theta_{13}^{(\ell)} \langle \sigma_1''^{(\ell)} \sigma_4'^{(\ell)} \sigma_2''^{(\ell)} \sigma_3'^{(\ell)} \rangle_{K^{(\ell)}} \\
&+ \frac{(C_W^{\ell+1})^2}{n_{\ell-1}} \langle \sigma_1'^{(\ell)} \sigma_4'^{(\ell)} \rangle_{K^{(\ell)}} \langle \sigma_2'^{(\ell)} \sigma_3'^{(\ell)} \rangle_{K^{(\ell)}} U_{1423}^{(\ell)}
\end{aligned} \tag{71}$$

E NTK mean at next to leading order

As discussed in section 3, the use of the Feynman rules introduced in the main text, and the selection rules of Appendix C constrain the number of diagrams one can construct for the case of two NTK external lines at leading order in $\frac{1}{n}$, to those displayed in (12).

Next, we provide the algebraic formulae associated to each diagram in such expansion:

$$\begin{aligned}
\frac{1}{n_{\ell-1}} \Theta^{(1)(\ell)} &= \frac{C_W^{(\ell+1)}}{n_{\ell-1}} \Theta_{12}^{\{1\}(\ell)} \langle \sigma_1'^{(\ell)} \sigma_2'^{(\ell)} \rangle_{K^{(\ell)}} \\
\frac{1}{n_{\ell-1}} K^{\{1\}(\ell)} &= \frac{1}{2n_{\ell-1}} \sum_{\beta_1, \beta_2 \in \{1,2\}} K_{\beta_1 \beta_2}^{\{1\}(\ell)} \left\langle \frac{d^2(\widehat{\Delta\Omega}_{12}^{(\ell+1)})}{dz_{\beta_1}^{(\ell)} dz_{\beta_2}^{(\ell)}} \right\rangle_{K^{(\ell)}}
\end{aligned}$$

$$\begin{aligned}
\frac{1}{n_{\ell-1}} V_4^{(\ell)} &= \frac{1}{n_{\ell-1}} \sum_{\beta_1, \beta_2, \beta_3, \beta_4 \in \{1,2\}} V_{(\beta_1 \beta_2)(\beta_3 \beta_4)}^{(\ell)} \left\langle \frac{d^4(\widehat{\Delta\Omega}_{12}^{(\ell+1)})}{dz_{\beta_1}^{(\ell)} dz_{\beta_2}^{(\ell)} dz_{\beta_3}^{(\ell)} dz_{\beta_4}^{(\ell)}} \right\rangle_{K^{(\ell)}} \\
\frac{1}{n_{\ell-1}} D_4^{(\ell)} &= \frac{C_W^{(\ell+1)}}{2n_{\ell-1}} \sum_{\beta_1, \beta_2 \in \{1,2\}} \left\langle \frac{d^2(\sigma'_1{}^{(\ell)} \sigma'_2{}^{(\ell)})}{dz_{\beta_1}^{(\ell)} dz_{\beta_2}^{(\ell)}} \right\rangle_{K^{(\ell)}} D_{\beta_1 \beta_2 12}^{(\ell)} \\
\frac{1}{n_{\ell-1}} F_4^{(\ell)} &= \frac{C_W^{(\ell+1)}}{n_{\ell-1}} \sum_{\beta_1, \beta_2 \in \{1,2\}} \left\langle \frac{d^2(\sigma'_1{}^{(\ell)} \sigma'_2{}^{(\ell)})}{dz_{\beta_1}^{(\ell)} dz_{\beta_2}^{(\ell)}} \right\rangle_{K^{(\ell)}} F_{\beta_1 \beta_2 12}^{(\ell)}
\end{aligned} \tag{72}$$

F Criticality analysis for NTK tensors

In this section, we will show that the tensors D , A and B , which describe the NTK statistics at leading order in $\frac{1}{n}$, as well as their higher-order generalizations, are also set to criticality once the susceptibilities of section 5.2 are constrained to satisfy (13), (16). We develop our analysis in the order mentioned above:

- (i) As discussed in 5.2, once the NNGP, quartic vertex and NTK are shown to be stable, the stability of the tensor D follows from the variation of the same tensor in the previous layer. In diagrams:

$$\begin{aligned}
&\text{Diagram: A central vertex with four legs labeled 1, 2, 3, 4. Legs 1 and 2 are solid black, legs 3 and 4 are dashed blue.} \\
&= \sum_{j_1, j_2} \text{Diagram: A chain of three circles. The first circle has legs 1 and 2. The second circle has legs 3 and 4. The third circle has legs 1 and 2. The chain is connected by wavy lines labeled } \widehat{\Delta G}_{j_1} \text{ and } z_{j_1}. \text{ The third circle has legs 3 and 4 labeled } \sigma'_{j_2} \sigma'_{j_2}.
\end{aligned} \tag{73}$$

or, in algebraic form

$$\frac{1}{n_{\ell}} \delta D_{1234}^{(\ell)} = \frac{1}{n_{\ell-1}} \sum_{\beta_1, \beta_2 \in \{1,2,3,4\}} (\chi_{||}^{(\ell+1)})_{12, \beta_1 \beta_2} (\chi_{\perp}^{(\ell+1)})_{34} \delta D_{\beta_1 \beta_2 34}^{(\ell)} \tag{74}$$

In this manner, one can see that the criticality conditions studied in the main text, namely $(\chi_{||}^{(\ell+1)})_{12, \beta_1 \beta_2} = \delta_{1\beta_1} \delta_{2\beta_2}$, $(\chi_{\perp}^{(\ell+1)})_{34} = 1$, immediately imply the stability of D .

- (ii) Analogously, one can study the stability of the NTK variance when the network has been set to criticality. In such a case, the variation of the tensor A at layer $\ell + 1$ readily follows from its corresponding recursive relation. In diagrams:

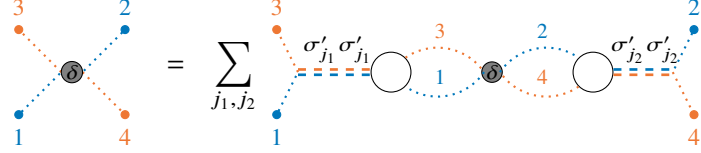
$$\begin{aligned}
&\text{Diagram: A central vertex with four legs labeled 1, 2, 3, 4. Legs 1 and 2 are solid blue, legs 3 and 4 are solid orange.} \\
&= \sum_{j_1, j_2} \text{Diagram: A chain of three circles. The first circle has legs 1 and 2. The second circle has legs 3 and 4. The third circle has legs 1 and 2. The chain is connected by wavy lines labeled } \sigma'_{j_1} \sigma'_{j_1} \text{ and } \sigma'_{j_2} \sigma'_{j_2}.
\end{aligned} \tag{75}$$

or, equivalently

$$\frac{1}{n_\ell} \delta A_{1234}^{(\ell)} = \frac{1}{n_{\ell-1}} (\chi_\perp^{(\ell+1)})_{12} (\chi_\perp^{(\ell+1)})_{34} \delta D_{1234}^{(\ell)} \quad (76)$$

Hence, we see that the criticality condition $(\chi_\perp^{(\ell+1)})_{\alpha\beta} = 1$, directly demands the stability of the tensor A .

(iii) In similar fashion, the variation of the tensor B under criticality conditions, reads



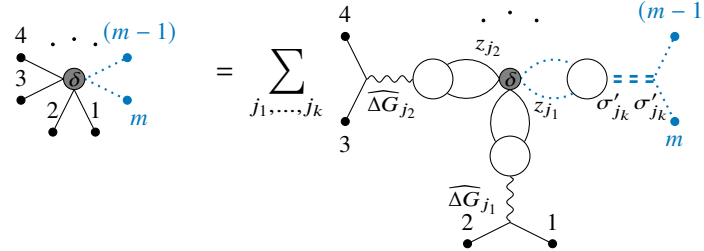
$$= \sum_{j_1, j_2} \dots \quad (77)$$

or, explicitly

$$\frac{1}{n_\ell} \delta B_{1324}^{(\ell)} = \frac{1}{n_{\ell-1}} (\chi_\perp^{(\ell+1)})_{13} (\chi_\perp^{(\ell+1)})_{24} \delta B_{1324}^{(\ell)} \quad (78)$$

Once more, one concludes that criticality, $(\chi_\perp^{(\ell+1)})_{\alpha\beta} = 1$, sets the stability of B .

(iv) One can now easily generalize our previous analysis of stability to higher-order tensors. Following our bootstrap strategy, the stability of the tensor $D_{1234\dots(m-1)m}^{(\ell+1)}$ in (17), can easily be deduced from the diagrammatic relation



$$= \sum_{j_1, \dots, j_k} \dots \quad (79)$$

which algebraically reads

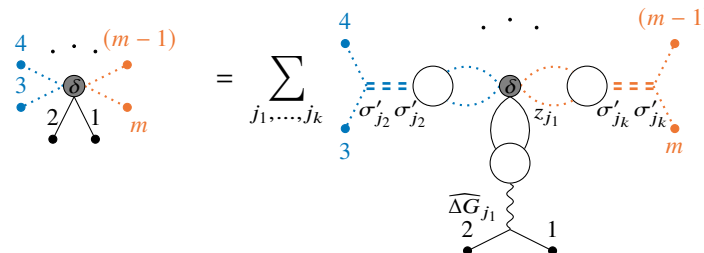
$$\delta D_{1234\dots(m-1)m}^{(\ell+1)} = \sum_{\beta_k} (\chi_{\parallel}^{(\ell+1)})_{12, \beta_1 \beta_2} (\chi_{\parallel}^{(\ell+1)})_{34, \beta_3 \beta_4} \dots (\chi_\perp^{(\ell+1)})_{(m-1)m} \delta D_{\beta_1 \beta_2 \beta_3 \beta_4 \dots (m-1)m}^{(\ell)} \quad (80)$$

Remarkably, one sees that the criticality conditions for χ_{\parallel} in (13) and χ_\perp below (19) are again sufficient to fix the stability of the tensor D .

(v) The higher-order generalization of the tensors A and B are obtained from the following expectation value involving two NTks:

$$\begin{aligned} & \mathbb{E}_\theta^c [z_{i_1,1}^{(\ell+1)}, z_{i_2,2}^{(\ell+1)}, \widehat{\Delta\Theta}_{i_3 i_4, 34}^{(\ell+1)}, \dots, \widehat{\Delta\Theta}_{i_{m-1} i_m, (m-1)m}^{(\ell+1)}] \\ &= \frac{1}{n_\ell^{\frac{m}{2}-1}} \left[\delta_{i_1 i_2} \delta_{i_3 i_4} \dots \delta_{i_{m-1} i_m} A_{1234\dots(m-1)m}^{(\ell+1)} + \delta_{i_1 i_2} \delta_{i_3 i_{(m-1)}} \dots \delta_{i_4 i_m} B_{123(m-1)\dots 4m}^{(\ell+1)} + \dots \right] \quad (81) \end{aligned}$$

The stability of the higher-order tensors A and B can easily be studied using our diagrammatic approach. The variation of the tensor A takes the form



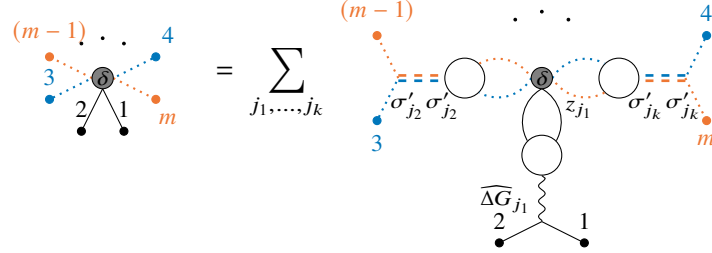
$$= \sum_{j_1, \dots, j_k} \dots \quad (82)$$

or, in analytical form

$$\delta A_{1234\dots(m-1)m}^{(\ell+1)} = \sum_{\beta_k} (\chi_{||}^{(\ell+1)})_{12,\beta_1\beta_2} (\chi_{\perp}^{(\ell+1)})_{34} \dots (\chi_{\perp}^{(\ell+1)})_{(m-1)m} \delta A_{\beta_1\beta_234\dots(m-1)m}^{(\ell)} \quad (83)$$

which shows A stays stable once the criticality conditions studied previously are satisfied.

Similarly, the variation of the tensor B reads



$$\delta B_{1234\dots(m-1)m}^{(\ell+1)} = \sum_{j_1, \dots, j_k} \dots \quad (84)$$

which translates into the formal expression

$$\delta B_{123(m-1)\dots 4m}^{(\ell+1)} = \sum_{\beta_k} (\chi_{||}^{(\ell+1)})_{12,\beta_1\beta_2} (\chi_{\perp}^{(\ell+1)})_{3(m-1)} \dots (\chi_{\perp}^{(\ell+1)})_{4m} \delta B_{\beta_1\beta_23(m-1)\dots 4m}^{(\ell)} \quad (85)$$

One sees again that the criticality conditions guarantee the stability of the higher-order tensor B .

G Proof of identities for scale-invariant nonlinearities

Scale-invariant activations functions are defined by

$$\sigma(z) = \begin{cases} a_+ z, & z \geq 0 \\ a_- z, & z < 0 \end{cases} \quad (86)$$

Due to its simplicity, one can evaluate Gaussian expectation values containing polynomials of these functions. For instance, the Gaussians $\langle \sigma(z)\sigma(z) \rangle_K$, $\langle \sigma'(z)\sigma'(z) \rangle_K$, which define the tensor $\widehat{\Delta\Omega}$ in 5.3, can be exactly computed through the use of ordinary algebraic manipulations. The former takes the form

$$\begin{aligned} \langle \sigma(z)\sigma(z) \rangle_K &= \frac{1}{\sqrt{2\pi K}} \int_{-\infty}^{+\infty} e^{-\frac{z^2}{2K}} \sigma^2(z) dz = \left(\frac{a_+^2 + a_-^2}{2} \right) \frac{1}{\sqrt{2\pi K}} \int_{-\infty}^{+\infty} e^{-\frac{z^2}{2K}} z^2 dz \\ &= A K \end{aligned} \quad (87)$$

where $A = \left(\frac{a_+^2 + a_-^2}{2} \right)$, while the latter results in

$$\begin{aligned} \langle \sigma'(z)\sigma'(z) \rangle_K &= \frac{1}{\sqrt{2\pi K}} \int_{-\infty}^{+\infty} e^{-\frac{z^2}{2K}} \sigma'^2(z) dz = \left(\frac{a_+^2 - a_-^2}{2} \right) \frac{1}{\sqrt{2\pi K}} \int_{-\infty}^{+\infty} e^{-\frac{z^2}{2K}} dz \\ &= \tilde{A} \end{aligned} \quad (88)$$

with $\tilde{A} = \left(\frac{a_+^2 - a_-^2}{2} \right)$.

Now it is straightforward to see that the Gaussian expectation value of the tensor $\widehat{\Delta\Omega}(z) = \sigma(z)\sigma(z) + C_W \Theta^{(l)} \sigma'(z)\sigma'(z)$ is given by

$$\langle \widehat{\Delta\Omega}(z) \rangle_K = AK + C_W \tilde{A} \Theta \quad (89)$$

which implies $\frac{d}{dK} \langle \widehat{\Delta\Omega}(z) \rangle = A$. This shows the validity of (20).

The equality (21) follows from ordinary integration techniques. Indeed,

$$\begin{aligned} 2K^2 \frac{d}{dK} \langle \sigma'(z) \sigma'(z) \rangle_K &= 2K^2 \frac{d}{dK} \left(\frac{1}{\sqrt{2\pi K}} \int_{-\infty}^{+\infty} e^{-\frac{z^2}{2K}} \sigma'^2(z) dz \right) \\ &= \int_{-\infty}^{+\infty} \frac{2K^2}{\sqrt{2\pi K}} \left(-\frac{1}{2K} + \frac{z^2}{2K^2} \right) \sigma'(z)^2 dz \\ &= \langle (z^2 - K) \sigma'(z) \sigma'(z) \rangle_K \end{aligned} \quad (90)$$

Thus, the Gaussian $\langle (z^2 - K) \sigma'(z) \sigma'(z) \rangle_K$ vanishes for scale-invariant nonlinearities, as discussed in 5.3.

H Additional experiments and details

H.1 Stability analysis

In this section we provide additional experiments verifying the simultaneous stability of the NNGP K , the four-point cumulant V_4 as well as the four tensors A, B, D and F with increasing network depth ℓ . Furthermore, we provide details of the numerical setup.

All experiments in this section are performed on a ReLU MLP without biases. For the inputs, each component of all vectors was drawn from a standard normal distribution. For the tensors A, B, D and F we thus used

$$x_0 = (-0.9895229339599609, -0.5992491841316223), \quad (91)$$

$$x_1 = (-0.17877478897571564, 2.253682851791382), \quad (92)$$

$$x_2 = (1.0237634181976318, -0.4618060886859894), \quad (93)$$

$$x_3 = (-0.5364212393760681, 1.9298086166381836). \quad (94)$$

For the two-dimensional tensors K and Θ , only x_0 and x_1 were used. For the V_4 computation, we used 4-dimensional inputs resulting in

$$x_0 = (-0.9895229339599609, -0.5992491841316223, -0.17877478897571564, +2.253682851791382), \quad (95)$$

$$x_1 = (+1.0237634181976318, -0.4618060886859894, -0.5364212393760681, +1.9298086166381836), \quad (96)$$

$$x_2 = (-1.95197594165802, -1.7220025062561035, +0.8821542859077454, -1.1963286399841309), \quad (97)$$

$$x_3 = (-0.1944112777709961, -0.540934145450592, +0.3308846354484558, +0.0907512903213501). \quad (98)$$

Monte-Carlo estimation of the kernels. The mean NTK and the mean NNGP are estimated by averaging over N_{net} initializations of the network, i.e.

$$\overline{K}_{\alpha\beta}^{(\ell)} = \frac{1}{N_{\text{net}}} \sum_{I=1}^{N_{\text{net}}} z_{I;i,\alpha}^{(\ell)} z_{I;i,\beta}^{(\ell)}, \quad (99)$$

$$\overline{\Theta}_{\alpha\beta}^{(\ell)} = \frac{1}{N_{\text{net}}} \sum_{I=1}^{N_{\text{net}}} \left(\sum_{\mu} \frac{\partial z_{I;i,\alpha}^{(\ell)}}{\partial \theta_{\mu}} \frac{\partial z_{I;i,\beta}^{(\ell)}}{\partial \theta_{\mu}} \right), \quad (100)$$

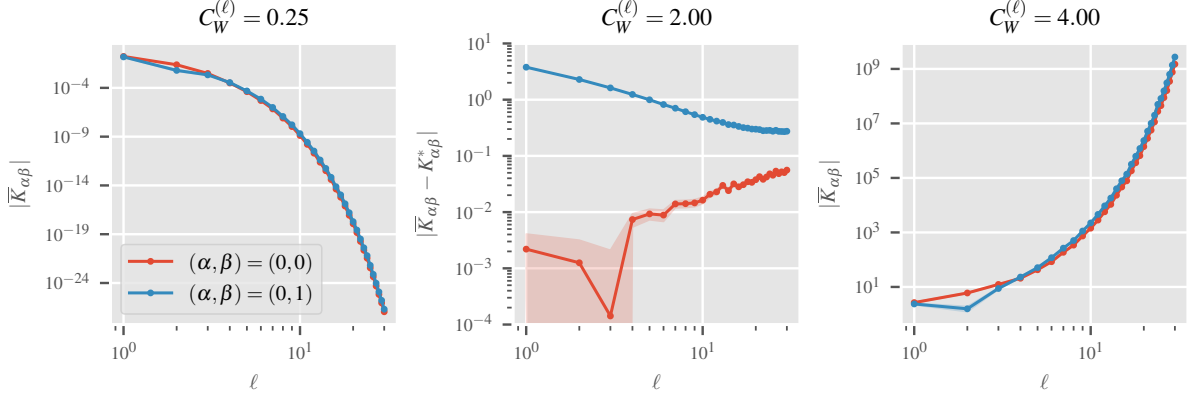


Figure 3: *Variance stability*. Components of the Monte–Carlo estimated NNGP $\overline{K}_{\alpha\beta}$ of a ReLU MLP as a function of layer depth ℓ corresponding to single and distinct inputs are shown for three different choices of $C_W^{(\ell)}$. The hidden layers are of size 200. The middle plot shows the deviation of the NNGP component to the predicted fixed point kernel $K_{\alpha\beta}^*$ at the critical value $C_W^{(\ell)} = C_W^c = 2$ (see text). Sample means are obtained from 1000 initializations for the non-critical cases (left and right), whereas the result in the middle is obtained from a sample size of $N_{\text{net}} = 10^6$. Error bars are included in all three plots (see text).

where i is an arbitrary but fixed channel in the corresponding layer and I labels the different initializations. The error bars correspond to the standard deviation of the mean and are estimated by dividing the sample standard deviation of the individual samples by $\sqrt{N_{\text{net}}}$. Due to the symmetries

$$V_{\alpha\beta\gamma\delta}^{(\ell)} = V_{\beta\alpha\gamma\delta}^{(\ell)} = V_{\alpha\beta\delta\gamma}^{(\ell)} = V_{\gamma\delta\alpha\beta}^{(\ell)}, \quad (101)$$

there are 55 independent components of this tensor. We compute the same subset as presented in [18].

Linear scaling of the NTK Θ at criticality. The purple line in Figure 1 (middle) shows the predicted linear scaling of the single-input NTK component for scale-invariant activation functions when setting $C_W^{(\ell)} = C_W^c$ [17]. For a bias-free ReLU MLP, it is given by

$$\Theta_{\alpha\alpha}^{(\ell)} = \frac{1}{n_0} \|x_\alpha\|^2 \ell. \quad (102)$$

Variance stability. For completeness, in Figure 3 we show the stability analysis of the variance corresponding to the same setup that was used for the gradient analysis shown in Figure 1, verifying the simultaneous stability of the NNGP and the NTK at the critical value C_W^c . Note that the variance has already been studied numerically in [18]. As argued in [17, 26, 18], there exists a non-trivial fixed point kernel $K_{\alpha\beta}^* \notin \{0, \infty\}$ for a ReLU MLP at criticality. It is given by

$$K_{\alpha\beta}^* = \frac{C_W^c}{n_0} \|x_\alpha\| \|x_\beta\|, \quad (103)$$

where n_0 denotes the dimension of the input space, and is subtracted from the estimated NNGP in Figure 3 (middle).

Monte–Carlo estimation of the four-point cumulant V_4 . Using (99), we estimate the four-point cumulant V_4 to first order by

$$\overline{V}_{\alpha\beta\gamma\delta}^{(\ell)} = \left(\frac{1}{N_{\text{net}}} \sum_{I=1}^{N_{\text{net}}} \frac{n_{\ell-1}}{n_\ell(n_\ell-1)} \sum_{\substack{i,j=1 \\ i \neq j}}^{n_\ell} z_{I;i,\alpha}^{(\ell)} z_{I;i,\beta}^{(\ell)} z_{I;j,\gamma}^{(\ell)} z_{I;j,\delta}^{(\ell)} \right) - n_{\ell-1} \overline{K}_{\alpha\beta}^{(\ell)} \overline{K}_{\gamma\delta}^{(\ell)} + O\left(\frac{1}{n}\right). \quad (104)$$

In contrast to (99), we exploit the fact here that all diagonal elements agree in expectation, i.e. we compute

$$\overline{K}_{\alpha\beta}^{(\ell)} = \frac{1}{N_{\text{net}}} \sum_{I=1}^{N_{\text{net}}} \frac{1}{n_{\ell}} \sum_{i=1}^{n_{\ell}} z_{I;i,\alpha}^{(\ell)} z_{I;i,\beta}^{(\ell)}. \quad (105)$$

In order to obtain statistics of this estimate, we repeat the Monte–Carlo sampling N_{stats} times (for both V_4 and K) and take the corresponding mean and standard deviation as the estimate for V_4 and its error, respectively. The results for up to $\ell = 30$ are shown in Figure 4 for the critical case and in Figure 5 for the non-critical case. In addition to the result in [18], we also provide regressions of the asymptotic power laws in the critical case, confirming the stability of V_4 .

Monte–Carlo estimation of the tensors A, B, D and F . Similarly to V_4 , the tensors are estimated to first order by

$$\overline{A}_{\alpha\beta\gamma\delta}^{(\ell)} = \frac{1}{N_{\text{net}}} \sum_{I=1}^{N_{\text{net}}} \frac{n_{\ell-1}}{n_{\ell}^2} \sum_{i,j=1}^{n_{\ell}} \widehat{\Delta\Theta}_{I;ii,\alpha\beta}^{(\ell)} \widehat{\Delta\Theta}_{I;jj,\gamma\delta}^{(\ell)} + O\left(\frac{1}{n}\right) \quad (106)$$

$$\overline{B}_{\alpha\gamma\beta\delta}^{(\ell)} = \frac{1}{N_{\text{net}}} \sum_{I=1}^{N_{\text{net}}} \frac{n_{\ell-1}}{n_{\ell}^2} \sum_{i,j=1}^{n_{\ell}} \widehat{\Delta\Theta}_{I;ij,\alpha\beta}^{(\ell)} \widehat{\Delta\Theta}_{I;ij,\gamma\delta}^{(\ell)} + O\left(\frac{1}{n}\right) \quad (107)$$

$$\overline{D}_{\alpha\beta\gamma\delta}^{(\ell)} = \frac{1}{N_{\text{net}}} \sum_{I=1}^{N_{\text{net}}} \frac{n_{\ell-1}}{n_{\ell}^2} \sum_{i,j=1}^{n_{\ell}} z_{I;i,\alpha}^{(\ell)} z_{I;i,\beta}^{(\ell)} \widehat{\Delta\Theta}_{I;jj,\gamma\delta}^{(\ell)} + O\left(\frac{1}{n}\right) \quad (108)$$

$$\overline{F}_{\alpha\gamma\beta\delta}^{(\ell)} = \frac{1}{N_{\text{net}}} \sum_{I=1}^{N_{\text{net}}} \frac{n_{\ell-1}}{n_{\ell}^2} \sum_{i,j=1}^{n_{\ell}} z_{I;i,\alpha}^{(\ell)} z_{I;j,\beta}^{(\ell)} \widehat{\Delta\Theta}_{I;ij,\gamma\delta}^{(\ell)} + O\left(\frac{1}{n}\right), \quad (109)$$

where the NTK fluctuation $\widehat{\Delta\Theta}_{ij,\alpha\beta}^{(\ell)}$ was already introduced in Section 3. Again, the computation is repeated N_{stats} times to obtain the mean and standard deviation of the estimate. For each of these tensors, the critical and non-critical cases are computed for the same input combinations as for V_4 up to $\ell = 30$. The results for tensor A are shown in Figures 6 & 7, for tensor B in Figures 8 & 9, for tensor D in Figures 10 & 11 and for tensor F in Figures 12 & 13. The regression of the asymptotic power laws is shown in blue for the critical cases. The power-law behavior at criticality for all tested components confirms that the NTK-tensors A, B, D and F are also stabilized by the critical initialization variance of the infinite width limit.

H.2 Kernel-corrections for other scale-invariant and scale-dependent activation functions

In the following we show the finite-width corrections for other activation functions than ReLU. We include two scale-invariant functions, namely the identity and the Leaky ReLU, and the scale-dependent GeLU activation to show the different qualitative behavior. For all activations functions, we used again inputs x_0 and x_1 given in (91) & (92)

Estimating the finite-width corrections. For a four-layer MLP without biases, we estimate the empirical NNGP according to (105) and the NTK according to

$$\overline{\Theta}_{\alpha\beta}^{(\ell)} = \frac{1}{N_{\text{net}}} \sum_{I=1}^{N_{\text{net}}} \left(\frac{1}{n_{\ell}} \sum_{i=1}^{n_{\ell}} \left(\sum_{\mu} \frac{\partial z_{I;i,\alpha}^{(\ell)}}{\partial \theta_{\mu}} \frac{\partial z_{I;i,\beta}^{(\ell)}}{\partial \theta_{\mu}} \right) \right). \quad (110)$$

The infinite-width solutions K and Θ (assuming NTK parametrization) is computed with the `neural-tangents` [10] library. Error estimates are obtained by dividing the sample variance of the estimated kernels by

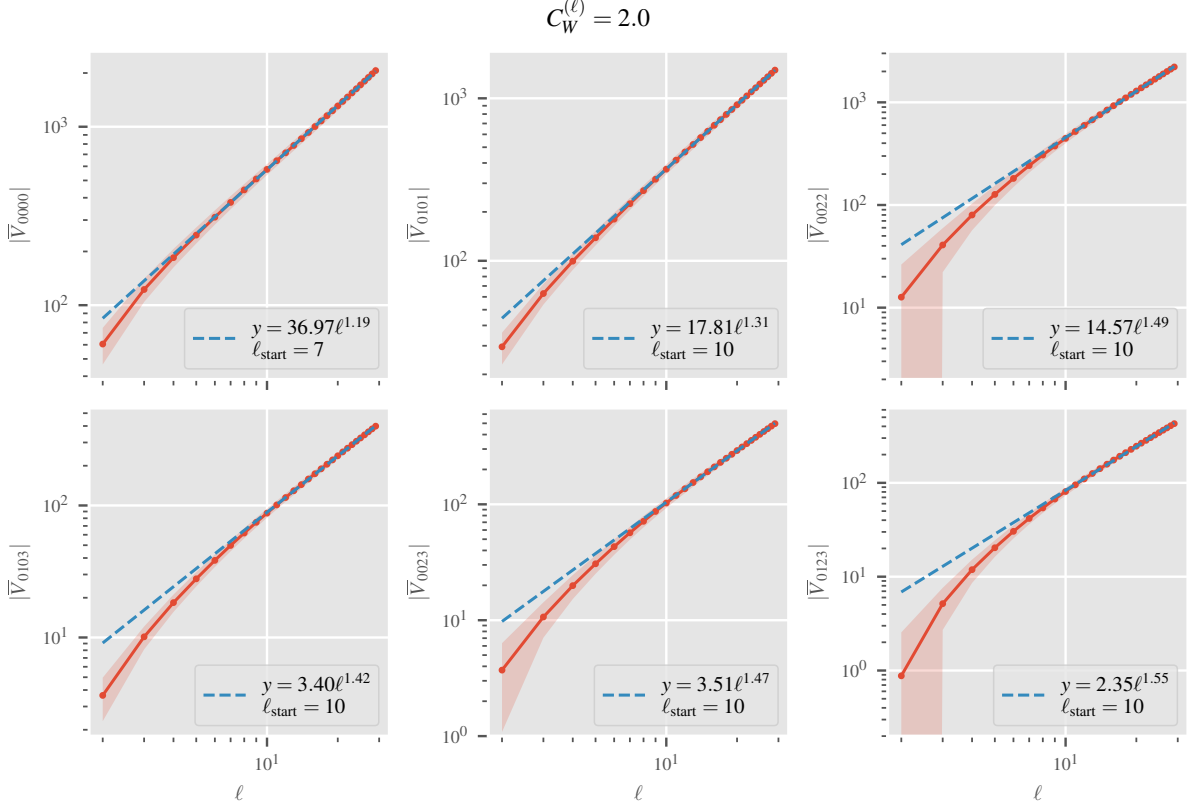


Figure 4: *Stability of the four-point cumulant V_4 at criticality.* Selected components of the Monte–Carlo estimated tensor \bar{V}_4 of a ReLU MLP as a function of layer depth ℓ are shown for the critical value $C_W^{(\ell)} = C_W^c = 2$. The hidden layers are of size 300. A regression of the asymptotic power law is shown in blue. The lowest layer included in the regression is given by ℓ_{start} . \bar{V}_4 is computed from $N_{\text{net}} = 10^4$ initializations and its mean and error bars are estimated from $N_{\text{stats}} = 1000$ repetitions (see text).

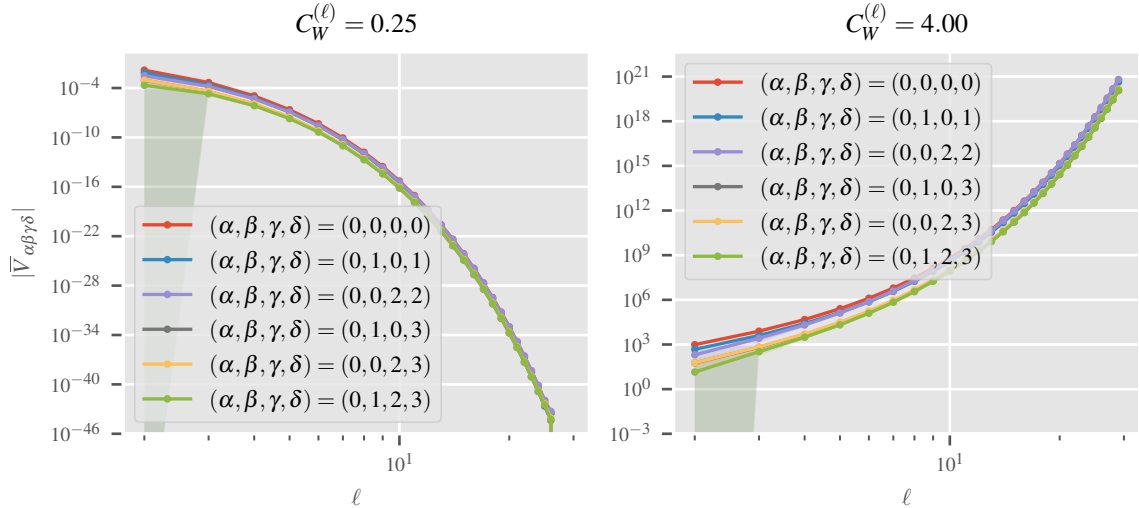


Figure 5: *Instability of the four-point cumulant V_4 away from criticality.* Selected components of the Monte–Carlo estimated tensor \bar{V}_4 are shown for $C_W^{(\ell)} < C_W^c$ (left) and $C_W^{(\ell)} > C_W^c$ (right). \bar{V}_4 is computed from $N_{\text{net}} = 10^4$ initializations and its mean and error bars are estimated from $N_{\text{stats}} = 1000$ repetitions (see text).

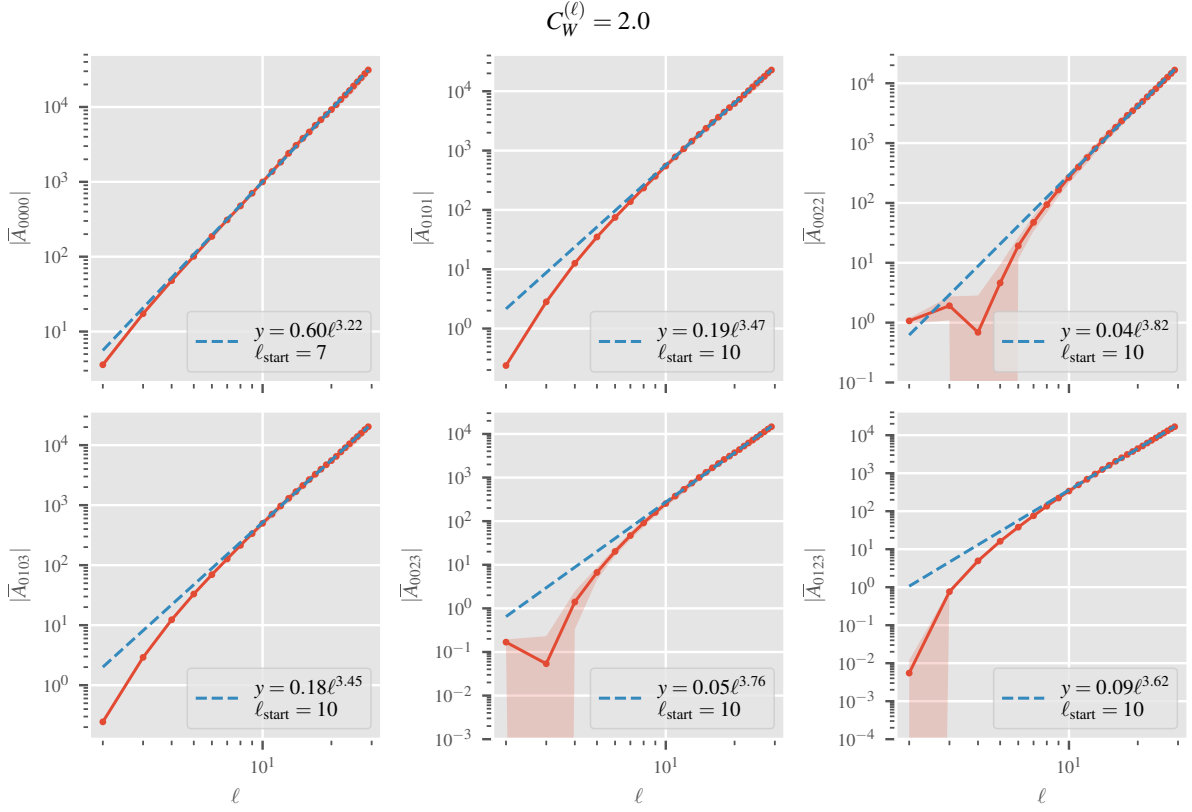


Figure 6: *Stability of the A tensor at criticality.* Selected components of the Monte–Carlo estimated tensor \bar{A} of a ReLU MLP as a function of layer depth ℓ are shown for the critical value $C_W^{(\ell)} = C_W^c = 2$. The hidden layers are of size 200. A regression of the asymptotic power law is shown in blue. The lowest layer included in the regression is given by ℓ_{start} . \bar{A} is computed from $N_{\text{net}} = 600$ initializations and its mean and error bars are estimated from $N_{\text{stats}} = 10$ repetitions (see text).

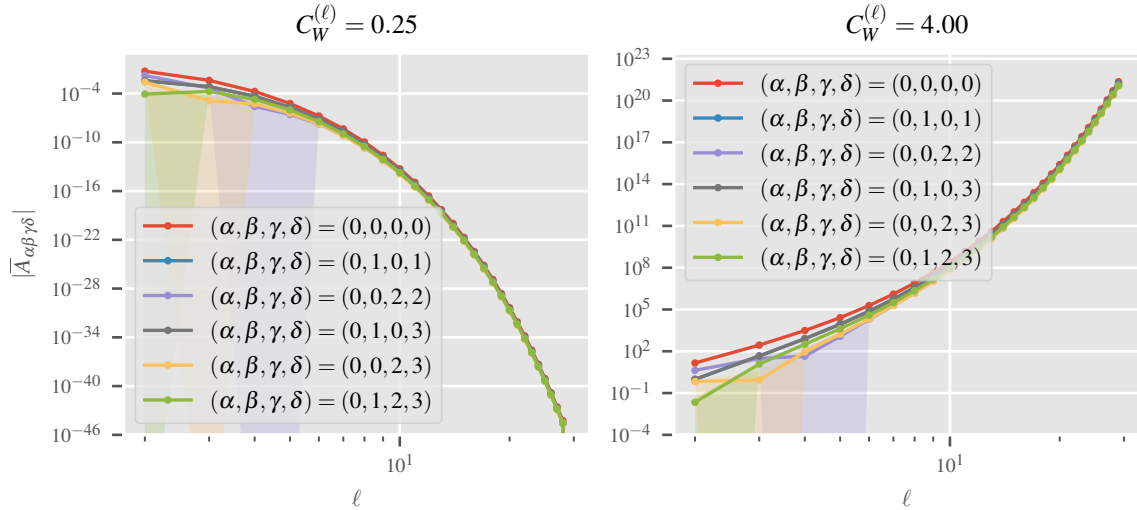


Figure 7: *Instability of the A tensor away from criticality.* Selected components of the Monte–Carlo estimated tensor \bar{A} are shown for $C_W^{(\ell)} < C_W^c$ (left) and $C_W^{(\ell)} > C_W^c$ (right). \bar{A} is computed from $N_{\text{net}} = 600$ initializations and its mean and error bars are estimated from $N_{\text{stats}} = 10$ repetitions (see text).

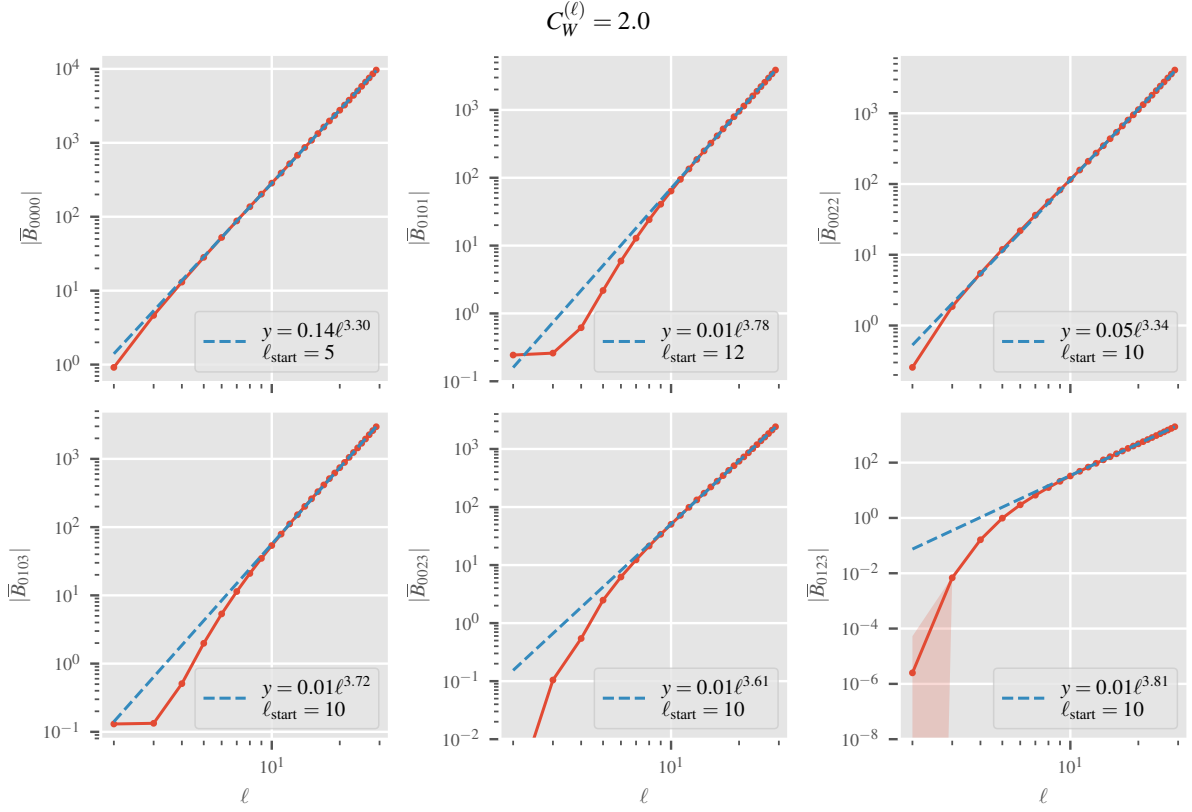


Figure 8: *Stability of the B tensor at criticality.* Selected components of the Monte–Carlo estimated tensor \bar{B} of a ReLU MLP as a function of layer depth ℓ are shown for the critical value $C_W^{(\ell)} = C_W^c = 2$. The hidden layers are of size 200. A regression of the asymptotic power law is shown in blue. The lowest layer included in the regression is given by ℓ_{start} . \bar{B} is computed from $N_{\text{net}} = 600$ initializations and its mean and error bars are estimated from $N_{\text{stats}} = 10$ repetitions (see text).

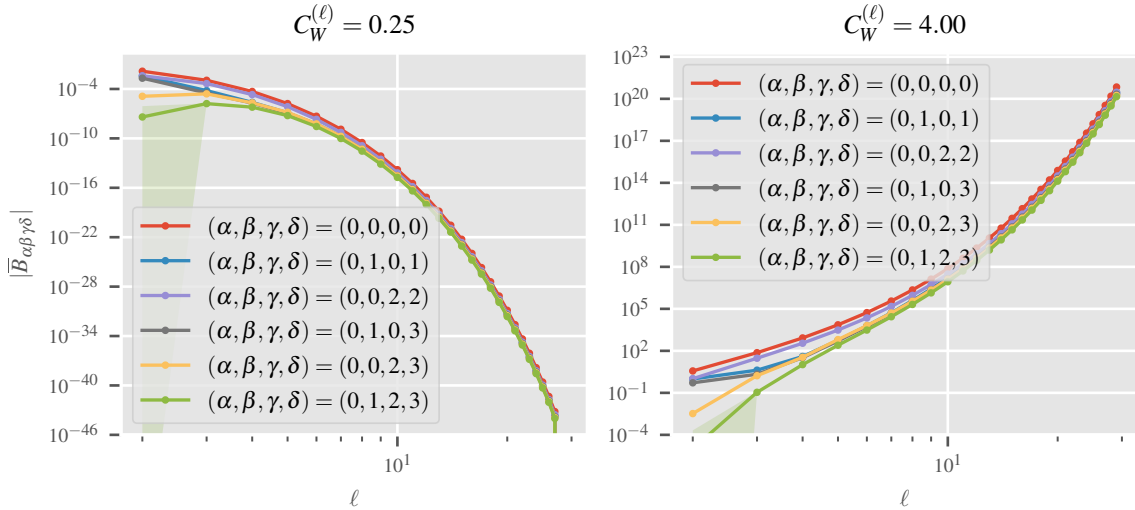


Figure 9: *Instability of the B tensor away from criticality.* Selected components of the Monte–Carlo estimated tensor \bar{B} are shown for $C_W^{(\ell)} < C_W^c$ (left) and $C_W^{(\ell)} > C_W^c$ (right). \bar{B} is computed from $N_{\text{net}} = 600$ initializations and its mean and error bars are estimated from $N_{\text{stats}} = 10$ repetitions (see text).

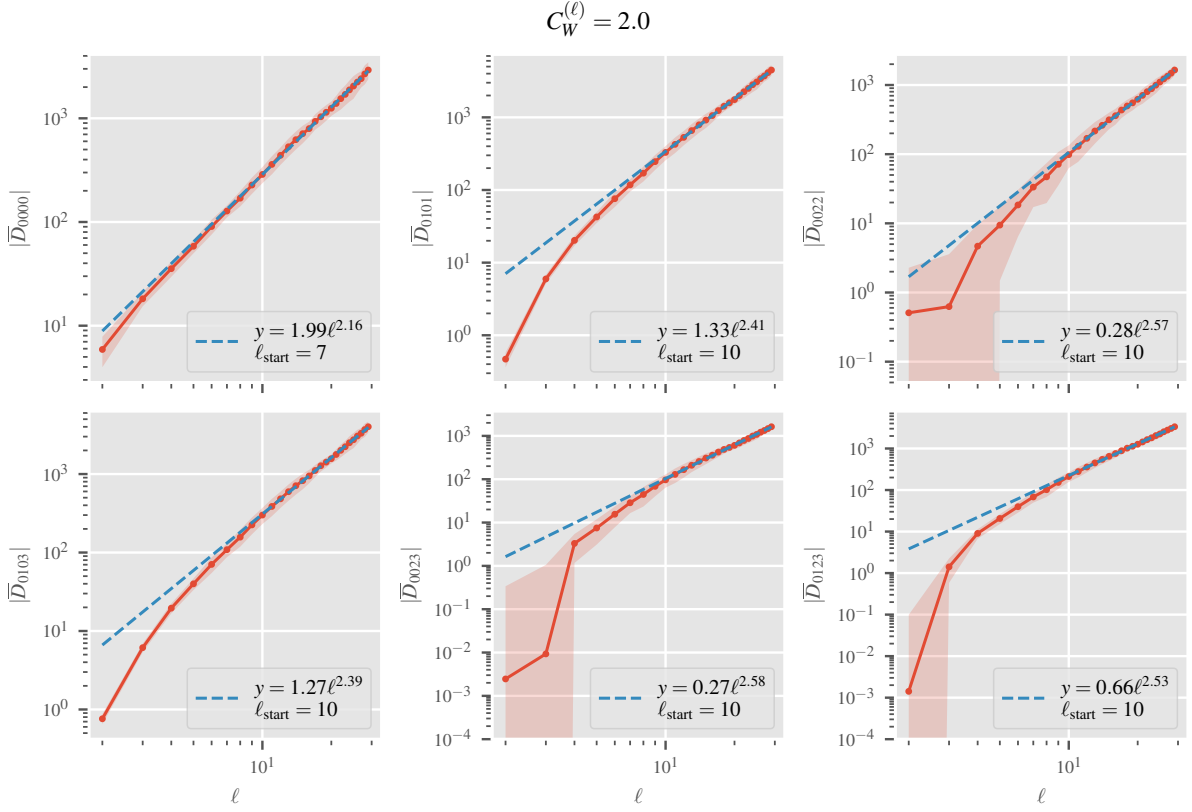


Figure 10: *Stability of the D tensor at criticality.* Selected components of the Monte–Carlo estimated tensor \bar{D} of a ReLU MLP as a function of layer depth ℓ are shown for the critical value $C_W^{(\ell)} = C_W^c = 2$. The hidden layers are of size 200. A regression of the asymptotic power law is shown in blue. The lowest layer included in the regression is given by ℓ_{start} . \bar{D} is computed from $N_{\text{net}} = 600$ initializations and its mean and error bars are estimated from $N_{\text{stats}} = 10$ repetitions (see text).

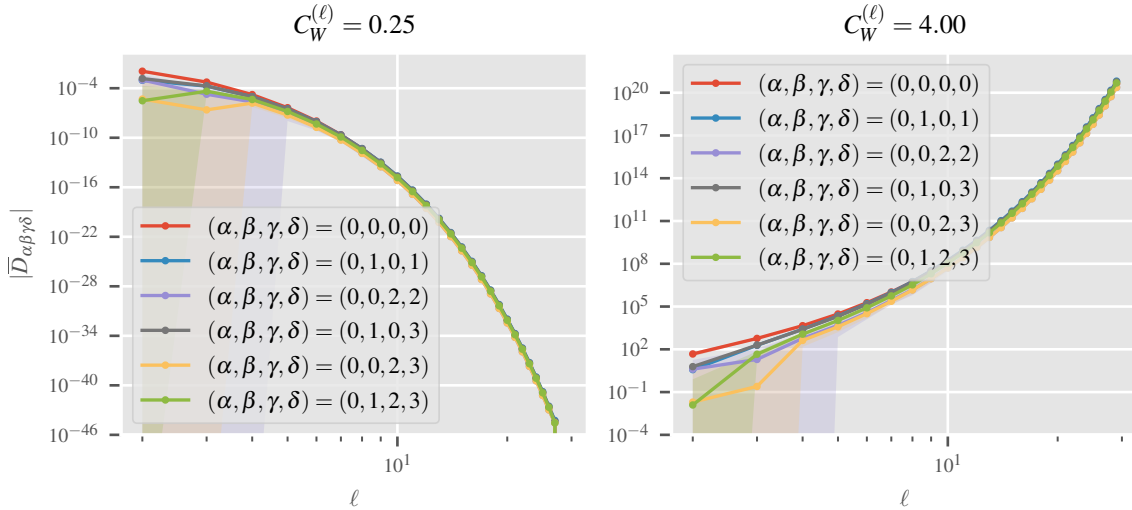


Figure 11: *Instability of the D tensor away from criticality.* Selected components of the Monte–Carlo estimated tensor \bar{D} are shown for $C_W^{(\ell)} < C_W^c$ (left) and $C_W^{(\ell)} > C_W^c$ (right). \bar{D} is computed from $N_{\text{net}} = 600$ initializations and its mean and error bars are estimated from $N_{\text{stats}} = 10$ repetitions (see text).

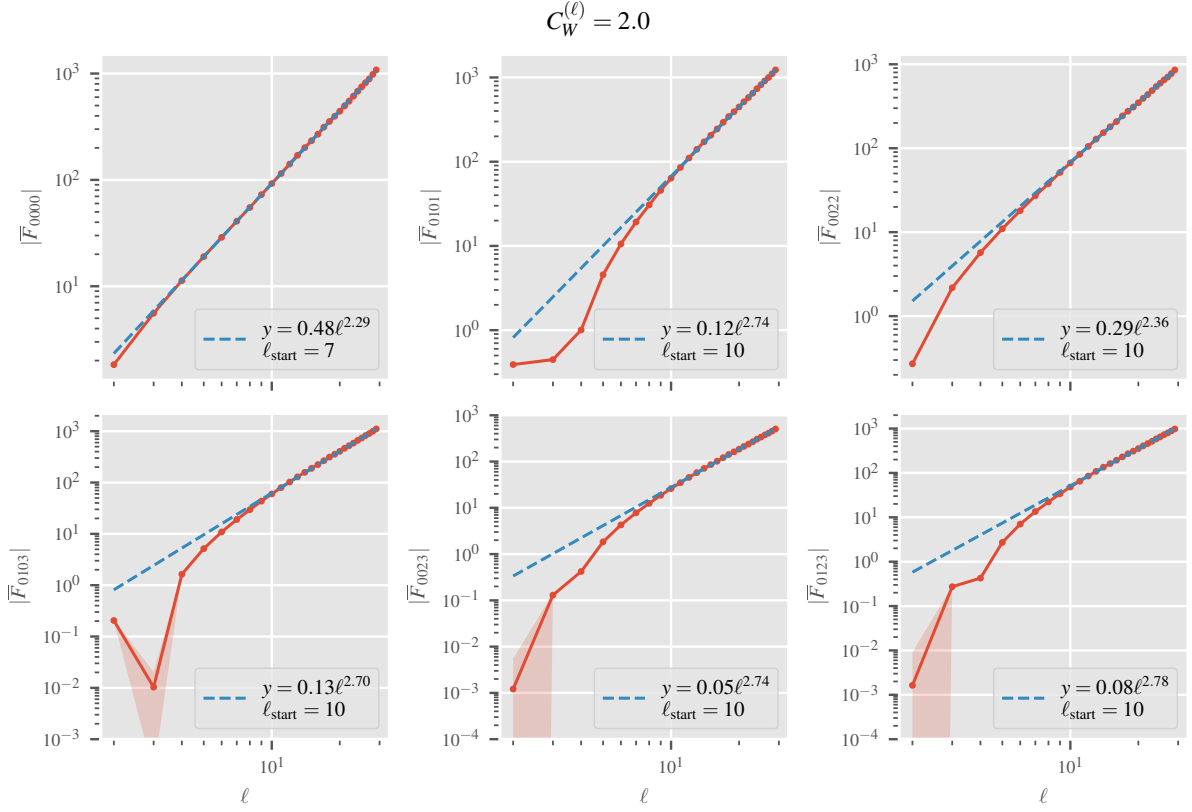


Figure 12: *Stability of the F tensor at criticality.* Selected components of the Monte–Carlo estimated tensor \bar{F} of a ReLU MLP as a function of layer depth ℓ are shown for the critical value $C_W^{(\ell)} = C_W^c = 2$. The hidden layers are of size 200. A regression of the asymptotic power law is shown in blue. The lowest layer included in the regression is given by ℓ_{start} . \bar{F} is computed from $N_{\text{net}} = 600$ initializations and its mean and error bars are estimated from $N_{\text{stats}} = 10$ repetitions (see text).

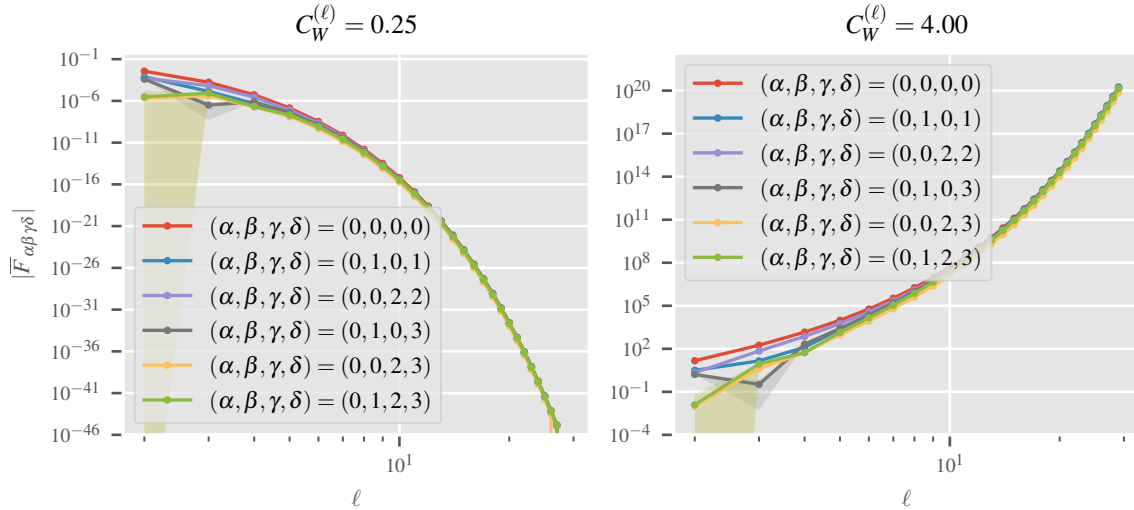


Figure 13: *Instability of the F tensor away from criticality.* Selected components of the Monte–Carlo estimated tensor \bar{F} are shown for $C_W^{(\ell)} < C_W^c$ (left) and $C_W^{(\ell)} > C_W^c$ (right). \bar{F} is computed from $N_{\text{net}} = 600$ initializations and its mean and error bars are estimated from $N_{\text{stats}} = 10$ repetitions (see text).

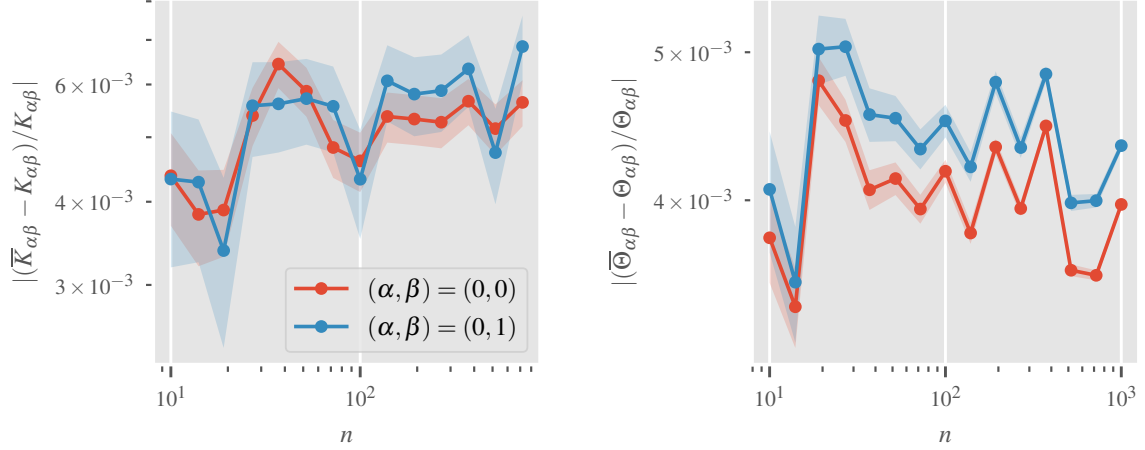


Figure 14: *Finite-width corrections for the identity.* Relative deviations of the Monte–Carlo estimated NNGP and NTK to its infinite-width counterparts as a function of hidden layer width $n = n_\ell$. A four layer linear MLP with $C_W = 2$ is sampled over 5×10^6 initializations. Error bars of the sample mean are included for all lines. Both a single and distinct input component of each kernel is shown.

$\sqrt{N_{\text{net}}}$ and further rescaling them by $1/K$ or $1/\Theta$, respectively, since we are considering the relative deviations.

The linear case. Using the identity as the activation function, we obtain the result in Figure 14. Both the single- and distinct-input component do not show any corrections with width, as expected. The variance of the weights is $C_W^{(\ell)} = 2$.

The Leaky ReLU case. Using

$$\sigma(x) = \alpha \min(x, 0) + \max(x, 0), \quad (111)$$

with $\alpha = 0.1$ as the activation function, we observe similar behavior as for the ReLU as can be seen in Figure 15. While the distinct-input component shows a convergence to the infinite-width limit, the single-input component is already exact at any finite width, as expected due to the scale-invariant nature. Again, $C_W^{(\ell)} = 2$.

The GeLU case. To show the distinct behavior of scale-dependent activation functions, we repeat the same experiment for the GeLU function. As shown in Figure 16, not only the distinct-input, but also the single-input component approach the infinite-width solution only with increasing width. Note that due to the scale-dependence, the scale of the input vectors affects the convergence behavior. Intuitively, large inputs emphasize the asymptotic regions of the activation function, rendering the corrections more similar to the ReLU case, whereas small inputs focus on the nearly linear region close to the origin, leading to a behavior similar to the linear case. Therefore, we rescaled the inputs x_0 and x_1 by a factor of 0.53 to make the distinct nature of this scale-dependent function more pronounced. The variance of the weights was set to $C_W^{(\ell)} = 1.98305826$ [17], in order to suppress significant change of magnitude of the preactivation values after a few layers.

H.3 Compute resources

All presented experiments were conducted on a cluster equipped with NVIDIA A40 GPUs with 48GB of RAM. The stability analysis for the NNGP and V_4 could each be computed on a single GPU in less than two hours for all three values of C_W . Tensors involving the gradient are more expensive to compute, thus

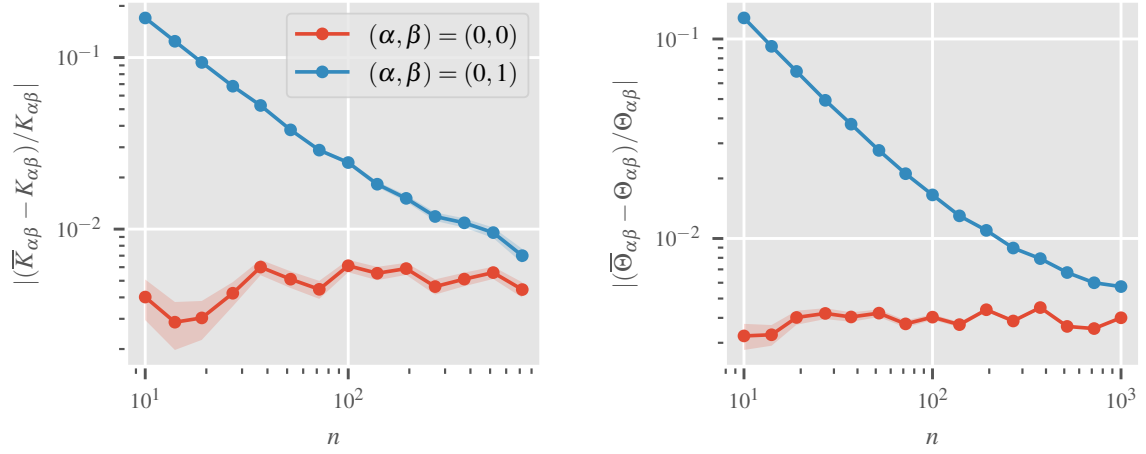


Figure 15: *Finite-width corrections for Leaky ReLU*. Relative deviations of the Monte–Carlo estimated NNGP and NTK to its infinite-width counterparts as a function of hidden layer width $n = n_\ell$. A four layer Leaky ReLU MLP with $C_W = 2$ is sampled over 5×10^6 initializations. Error bars of the sample mean are included for all lines. Both a single and distinct input component of each kernel is shown.

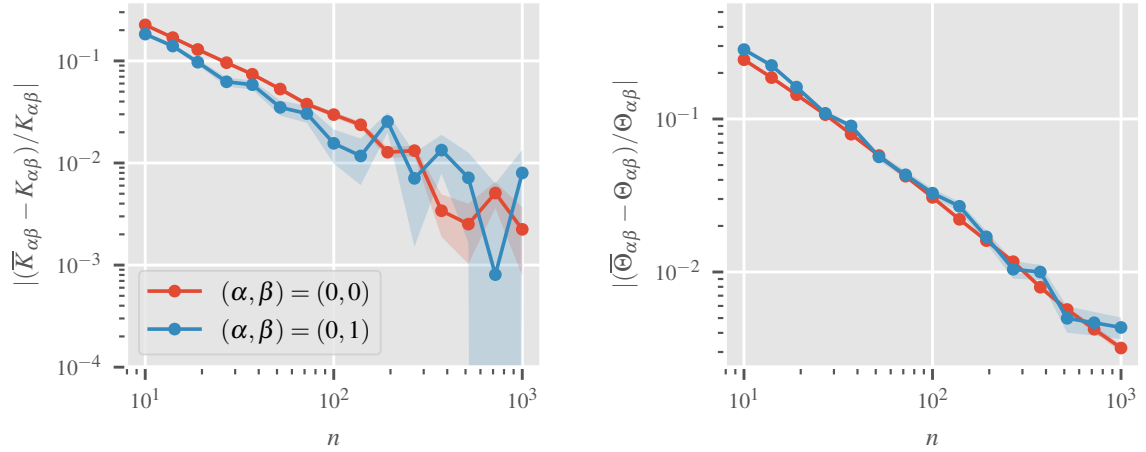


Figure 16: *Finite-width corrections for GeLU*. Relative deviations of the Monte–Carlo estimated NNGP and NTK to its infinite-width counterparts as a function of hidden layer width $n = n_\ell$. A four layer GeLU MLP with $C_W = 2$ is sampled over 5×10^5 initializations. Error bars of the sample mean are included for all lines. Both a single and distinct input component of each kernel is shown.

the layer width was reduced to 200. On a single GPU, a single such tensor for three different values of C_W was computed in less than 6 hours. Note that multiple tensors can be computed in parallel using the same ensemble.

Similarly, the finite-width corrections are fast to compute for the NNGP but more expensive for the NTK. For each activation function, it took less than three hours to obtain the results presented here.

I D tensor at next-to-next-to leading order from Feynman diagrams

In this Appendix we display all the possible diagrams that can be built out of the Feynman rules defined in **C**, for the specific case of the tensor D in the expectation value

$$\begin{aligned} \mathbb{E}_\theta^c [z_{i_1,1}^{(\ell+1)}, z_{i_2,2}^{(\ell+1)}, z_{i_3,3}^{(\ell+1)}, z_{i_4,4}^{(\ell+1)}, \widehat{\Delta\Theta}_{i_5 i_6, 56}^{(\ell+1)}] \\ = \frac{1}{n_\ell^2} \left[\delta_{i_1 i_2} \delta_{i_3 i_4} \delta_{i_5 i_6} D_{123456}^{(\ell+1)} + \delta_{i_1 i_2} \delta_{i_3 i_5} \delta_{i_4 i_6} F_{123546}^{(\ell+1)} + \dots \right] \end{aligned} \quad (112)$$

The diagrams describing the tensor D at layer $\ell + 1$ are then given by

$$\begin{aligned} \frac{1}{n_\ell} D_{123456}^{(\ell+1)} = & \sum_j \left(\text{Diagram 1} \right) + \sum_{j_1, j_2} \left(\text{Diagram 2} \right) + P(12, 34, 56) \\ & + \sum_{j_1, j_2, j_3} \left(\text{Diagram 3} \right) + P(12, 34, 56) \\ & + \sum_{j_1, j_2, j_3} \left(\text{Diagram 4} \right) + \sum_{j_1, j_2, j_3} \left(\text{Diagram 5} \right) \\ & + \sum_{j_1, j_2, j_3} \left(\text{Diagram 6} \right) + P(12, 34) \end{aligned}$$

The diagrams are Feynman diagrams representing the tensor D at layer $\ell + 1$. They consist of vertices (circles) and edges (wavy lines). The vertices are labeled with indices j_1, j_2, j_3 and the edges are labeled with ΔG_j and $\Delta \Omega_j$. The diagrams are arranged in a large equation, with each term representing a different Feynman diagram. The diagrams are connected by plus signs and the entire expression is enclosed in large parentheses.

$$\begin{aligned}
& + \sum_{j_1, j_2} \left(\text{Diagram 1} + P(12, 34) + \text{Diagram 2} \right) \\
& + \sum_{j_1, j_2} \text{Diagram 3}
\end{aligned} \tag{113}$$

The diagrams are Feynman-like graphs with vertices labeled 1 through 6. Diagram 1 (inside the first sum) shows a vertex 1 connected to 2 and 3, with a wavy line labeled ΔG_{j_1} connecting to a loop structure involving ϕ_{j_2} and σ'_{j_1} , which then connects to vertex 6. Diagram 2 (inside the first sum) is similar but with a different loop structure. Diagram 3 (in the second sum) shows a more complex structure with multiple loops and vertices.

where $P(a_1 a_2, a_3 a_4, \dots, a_{2k-1} a_{2k})$ denotes the complement of the set of permutations generated by the pairs $(a_1 a_2), (a_3 a_4), \dots, (a_{2k-1} a_{2k})$, e.g. $P(12, 34) = \{(34, 12)\}$.

We have checked that these diagrams successfully reproduce the formulae obtained from perturbation theory and functional integration when applied to the study of the statistics of the NTK at order $\frac{1}{n^2}$.